A&A 538, A82 (2012)
DOI: 10.1051/0004-6361/201117402

Astronomy & Astrophysics

The dynamical and chemical evolution of dwarf spheroidal galaxies with GEAR⋆

Y. Revaz[1] and P. Jablonka[1,2]

[1] Laboratoire d'Astrophysique, École Polytechnique Fédérale de Lausanne (EPFL), 1290 Sauverny, Switzerland
e-mail: yves.revaz@epfl.ch
[2] GEPI, Observatoire de Paris, CNRS UMR 8111, Université Paris Diderot, 92125 Meudon Cedex, France

Received 3 June 2011 / Accepted 31 August 2011

ABSTRACT

We present the fully parallel chemo-dynamical Tree/SPH code GEAR, which allows us to perform high resolution simulations with detailed chemical diagnostics. Starting from the public version of Gadget-2, we included the complex treatment of the baryon physics: gas cooling, star formation law, chemical evolution, and supernova feedback. We qualified the performances of GEAR in the case of dwarf spheroidal galaxies (dSphs) galaxies. Our code GEAR conserves the total energy budget of the systems to better than 5% over 14 Gyr and provides an excellent convergence of the results with numerical resolution. We showed that models of dSphs in a static Euclidean space, where the expansion of the universe is neglected are valid. In addition, we tackled some existing open questions in the field, such as the stellar mass fraction of dSphs and its link to the predicted dark matter halo mass function, the effect of supernova feedback, the spatial distribution of the stellar populations, and the origin of the diversity in star formation histories and chemical abundance patterns. Strong supernova-driven winds seem incompatible with the observed metallicities and luminosities. Despite newly formed stars being preferentially found in the galaxy central parts, turbulent motions in the gas can quickly erase any metallicity gradient. The diversity in properties of dSph are related to a range of total masses, as well as a range of dispersion in the central densities, which is also seen in the halos emerging from a ΛCDM cosmogony.

Key words. galaxies: evolution – dark matter – galaxies: dwarf – galaxies: abundances – galaxies: formation – galaxies: star formation

1. Introduction

The first motivation behind the present work was to improve on our previous study in Revaz et al. (2009), which sought to identify the dominant physical processes at the origin of the dynamical and chemical properties of dSphs. While allowing a critical step forward with a large set of simulations, the excellence of the treeAsph code used in this work was somewhat diminished by its serial numerical structure (Serna et al. 1996; Alimi et al. 2003), hampering the possibility of high resolution simulations, which require large amounts of computing time.

The analysis of other Tree/SPH codes, which include chemical evolution schemes and have been applied to the formation and evolution of dwarf galaxies, demonstrates that the specific astrophysical aims of each study influence if not control the numerical implementations. Using color-magnitude diagrams as observational probes, Carraro et al. (2001) modeled their gas particles as closed box models and used the instantaneous recycling approximation. Marcolini et al. (2006, 2008) focused on the response of the ISM to the supernova explosion and introduced an arbitrary number of star formation episodes. Kawata et al. (2006), following Kawata & Gibson (2003), combined kinetic and thermal feedbacks, which could generate galactic winds in elliptical galaxies. Okamoto et al. (2010) investigated the effect of different recipes for the kinetic feedback driving galactic winds, on the global properties of the Milky Way satellite model galaxies. Read et al. (2006) looked for a mass boundary distinguishing between essentially pure dark halos and small stellar systems. They chose a unique global yield reproducing the metallicity of the inter-galactic medium at $z = 3$. Stinson et al. (2007) and Governato et al. (2010) applied the Stinson et al. (2006)'s blast wave recipe for the feedback. Sawala et al. (2010) used the multiphase scheme for the interstellar medium developed by Scannapieco et al. (2005, 2006), and constrained the fraction of metals given to the cold gas phase, later defining the final metallicity for a given stellar mass, on the metallicity-relation of dwarf galaxies. Valcke et al. (2008) and later Schroyen et al. (2011) took into account stellar winds and supernova explosions but only considered the global metallicity Z. Ricotti & Gnedin (2005) stopped their simulations very early on ($z \sim 8$) but included continuum radiative transfer to compare the global properties of dSphs with a simulated sample of galaxies formed before reionization.

We developed a new N-body code, hereafter GEAR, to fulfill a number of requirements including the capability of offering high spatial resolution together with detailed chemical diagnostics, and following the galaxy evolution over a full Hubble time, either in isolation or in a cosmological context. Because our approach to constraining the scenarios of galaxy evolution involves confrontation with observed stellar metallicity distributions and stellar abundance ratios, we carefully evaluated the impact of the supernova feedback on these quantities, and probed all ingredients in the parametrization of the star formation. While it would be very difficult to follow in detail the star formation processes on the scale of molecular clouds, we tried nevertheless to avoid as much as possible ad hoc assumptions, and based our modeling on purely physical grounds. Great care was devoted to tracing all sources and sinks of energy and guaranteeing an accurate budget of gains and losses. We also controlled the convergence of the results.

⋆ Appendices A and B are available in electronic form at http://www.aanda.org

The code GEAR is a flexible fully parallel chemo-dynamical Tree/SPH code, which we applied to tackle some of the questions that were left open after Revaz et al. (2009), such as the gas motions and the final radial distribution of the stellar population in dwarf spheroidal galaxies. It also allowed us to expand on a number of new subjects, in particular the question of the relation between galaxies in isolation and their parent halos in cosmological simulations, and clarify the final baryonic fraction of galaxies as a function of their halo masses.

The paper is organized as follows: the code and the implementation of physical processes are described in Sect. 2. The initial conditions are detailed in Sect. 3. The robustness of the code is discussed in Sect. 4. The role and impact of the main parameters are evaluated in Sect. 5, while Sect. 6 focuses on the initial mass and central gas density. Section 7 describes the different regimes of star formation for low mass galaxies and makes the first detailed comparison with the observations. Section 8 addresses the question of the spatial distribution of the stellar population as a function of their age and metallicity. Section 9 investigates the link between stellar masses in galaxies and their parent dark matter halos. Section 10 summarizes our results.

2. GEAR

We supplemented the public version of Gadget-2 (Springel 2005) with the complex treatment of the baryon physics incorporating: gas cooling, a star formation law, chemical evolution, and supernova feedback.

2.1. The gas cooling

The interstellar medium (ISM) is modeled as an ideal, inviscid gas with an adiabatic index $\gamma = 5/3$. The continuity equation is inserted into the first law of thermodynamics in order to follow the evolution of the gas specific internal energy. The variation in the internal energy depends on the mechanical forces, the artificial viscosity, and the radiative cooling expressed through a cooling function $\Lambda(\rho, T)$. Following the integration scheme of Gadget-2, we use the entropy function A (see Springel & Hernquist 2002, for the exact definition) instead of the internal energy as an independent thermodynamic variable. The variation in A is simplified as a sum of two terms corresponding to the contributions of the artificial viscosity (Springel 2005) and the cooling

$$\frac{\mathrm{d}}{\mathrm{d}t}A = \frac{\mathrm{d}}{\mathrm{d}t}A\Big)_{\mathrm{visc}} + \frac{\mathrm{d}}{\mathrm{d}t}A\Big)_{\mathrm{cool}}, \tag{1}$$

where:

$$\frac{\mathrm{d}}{\mathrm{d}t}A\Big)_{\mathrm{cool}} = -(\gamma - 1)\,\rho^{-\gamma}\,\Lambda(\rho, T). \tag{2}$$

For temperatures hotter than 10^4 K, the cooling function is calculated following the metallicity-dependent prescription of Sutherland & Dopita (1993). Below 10^4 K, the cooling of H_2 and HD molecules are taken into account as well as the atoms of oxygen, carbon, silicon, and iron (Maio et al. 2007). We refer to Revaz et al. (2009) for more details.

In dense ($\rho > 0.01\,\mathrm{m_H/cm^3}$) and warm-hot regions ($T > 10^4$ K), the cooling time may be much shorter than the dynamical time requiring extremely short time steps. In such a case, we use the isochoric approximation (see for example, Springel et al. 2001), assuming a constant density ρ. The integration of Eq. (1) is performed using adaptive time steps set to a fraction of 2% of the cooling time defined as

$$t_{\mathrm{cool}} = \frac{A}{\frac{\mathrm{d}}{\mathrm{d}t}A)_{\mathrm{cool}}}. \tag{3}$$

We do not take into account the heating of the gas by a cosmic background UV field. Its effect was investigated in a number of former studies (e.g., Sawala et al. 2010; Okamoto et al. 2010), because it could contribute to evaporating the gas in small halos ($v_{\mathrm{max}} \leq 12\,\mathrm{km\,s^{-1}}$).

However, the ISM is known to be strongly inhomogeneous down to very small scales, reaching densities $\sim 10^6\,\mathrm{m_H/cm^3}$ (e.g., Omont 2007; Beuther et al. 2007, and references therein), for which the cooling time is very short. When these overdensities cannot be properly resolved, the inclusion of an additional heating source, such as the UV background may no be the correct approach, because the cooling will be underestimated owing to the lack of resolution. This will be true regardless of whether we take into account that the gas may be self-shielded, strongly complicating the effect of the UV field. In this picture, improving the cooling by following precisely all cooling agents involved is also unprofitable. As no heating process is taken into account here, the integration of Eq. (1) is unaffected by numerical instabilities and an implicit integration scheme is not required.

2.2. Star formation law

Complex and poorly understood star formation processes are implemented using the phenomenological prescription proposed by Katz (1992) and Katz et al. (1996).

A gas particle becomes eligible to star formation when it fulfills the following physical conditions: *i*) the particle is collapsing (its velocity divergence is negative); *ii*) its density is higher than a threshold ρ_{sfr}; and *iii*) its temperature is lower than a threshold T_{sfr}.

In a time interval Δt, an eligible gas particle of mass m_{g} has a probability $p_\star$ of forming a stellar particle of mass $m_\star$ (Springel & Hernquist 2003)

$$p_\star = \frac{m_{\mathrm{g}}}{m_\star}\left[1 - \exp\left(-\frac{c_\star}{t_{\mathrm{g}}}\Delta t\right)\right], \tag{4}$$

where $c_\star$ is the star formation parameter and t_{g} the local free-fall time. This ensures that the star formation law is independent of both the time step Δt and $m_\star$

$$\frac{\mathrm{d}\rho_\star}{\mathrm{d}t} = \frac{c_\star}{t_{\mathrm{g}}}\rho_{\mathrm{g}}, \tag{5}$$

in which ρ_{g} is the gas density.

Each gas particle can form a number of stellar particles, this number is set by the parameter $N_\star$. Each new stellar particle represents an ensemble of stars sampling an initial mass function (IMF) with different slopes, α, in four stellar mass ranges (Kroupa 2001), taking into account the systematic effects caused by unresolved binaries

$$\alpha = \begin{cases} -0.3, & \text{if} \quad m < 0.08\,M_\odot \\ -1.8, & \text{if} \quad 0.08\,M_\odot < m < 0.50\,M_\odot \\ -2.7, & \text{if} \quad 0.50\,M_\odot < m < 1.00\,M_\odot \\ -2.3, & \text{if} \quad m > 1.00\,M_\odot. \end{cases} \tag{6}$$

The minimal and maximal stellar masses, which are considered in the definition of the IMF, are 0.05 and 50 $M_\odot$, respectively.

The stellar particles are assigned the positions, velocities, and chemical abundances of their parent gas particles. These gas and stars are dynamically decoupled, hence their evolution in phase space quickly diverges.

In GEAR, the stellar particles are numerically considered as an independent class of particles with their own structure. This is necessary to optimize the memory needed to store their chemical properties. The code GEAR still enables all types of particles to be ordered following the Peano-Hilbert curve in a similar way to Gadget-2. This allows us to take advantage of the fast cache-memory available on modern processors.

We set $T_{\rm sfr}$ to $3{\times}10^4$ K. The precise value of $T_{\rm sfr}$ is not important, and is chosen here to avoid the formation of stars in hot gas. The other parameters, $c_\star$, $\rho_{\rm sfr}$, and the maximal number of stellar particles that may be created from one gas particle $N_\star = m_{\rm g}/m_\star$ are discussed in detail in Sect. 5.

2.3. Chemical evolution

The galactic evolution is influenced by two main features of the stellar evolution: nucleosynthesis, and stellar feedback (winds or supernova explosions). In the following, we only consider the effects of supernovae, because the stellar winds from intermediate mass stars inject much less power into the ISM (Leitherer et al. 1992). Moreover, the evolution of the galactic systems that we consider is already well constrained by the abundances of both the α-elements (magnesium) and iron and their ratios. These elements are produced by Type Ia (SNeIa) and Type II (SNeII) supernovae.

For a given stellar particle, the number of stars ending their lifetime is computed at each dynamical time step. These stellar lifetimes depend on the metallicity at the creation of the particle and are taken from Kodama & Arimoto (1997, priv. comm.). To achieve a sufficiently accurate time resolution, we impose a maximum time step of 0.2 Myr. This corresponds to less than 10% of the smallest lifetime of the exploding stars in our simulation (about 3 Myr). The stellar-mass-dependent yields of SNeII for stars between 8 and 50 $M_\odot$ are taken from Tsujimoto et al. (1995). We adopt the model of Kobayashi et al. (2000) for the explosion of SNeIa. The progenitors of SNeIa have main-sequence masses between 3 and 8 $M_\odot$, and evolve into C+O white dwarfs (WDs). These white dwarfs can form two different types of binary systems, either with main sequence stars or with red giants (see Revaz et al. 2009, for more the details about the adopted parameters). The nucleosynthesis products of SNeIa are taken from the model W7 of Iwamoto et al. (1999). In contrast to Kobayashi et al. (2000), we do not prevent SNeIa explosions at [Fe/H] below -1. We note that the nucleosynthesis tables and the IMF can easily be changed in GEAR.

The stellar chemical ejecta are distributed among the nearest neighbors following the SPH scheme (e.g., Wiersma et al. 2009; Revaz et al. 2009). First, the gas density ρ_i and corresponding smoothing length h_i are determined at the location of each stellar particle i. Both quantities are computed similarly to the case of the gas particles (Springel 2005). The mass of metals ejected from particle i and attributed to particle j is computed through the weights w_{ij}

$$w_{ij} = \frac{m_j W(r_{ij}, h_i)}{\rho_i}, \tag{7}$$

where W is the SPH kernel function, m_j is the mass of the particle j, and r_{ij} is the distance between the particles i and j. By default, the number of neighbors used is set to $N_{\rm ngb} = 50$. The effect of varying $N_{\rm ngb}$ is discussed in Sect. 5.6. To improve the conservation of energy during the process of mass ejection, the velocities and the entropy of the particles are modified as described in Appendix A.

The chemical abundances are calculated with respect to the solar abundances of Anders & Grevesse (1989). The V-band luminosities are derived following the stellar population synthesis model of Vazdekis et al. (1996) computed for the revised Kroupa (2001) IMF. Where necessary, the luminosities are inter- and extra-polated in age and metallicity using a bi-variate spline.

2.4. Feedback

Each supernova explosion injects an energy $\epsilon_{\rm SN} \cdot E_{\rm SN}$ into the ISM, with $E_{\rm SN} = 10^{51}$ erg and $\epsilon_{\rm SN}$ the feedback efficiency factor, as discussed later in Sect. 5.1.

The supernova explosion feedback is definitively a complex mechanism, which has led to number of reports discussing both its numerical implementation and its physical operation modes. One can broadly define three different types of methods that are discussed in the literature. The so-called thermal feedback energy is released through the heating of the gas, in either homogeneous ISM (Gerritsen 1997; Mori et al. 1997; Thacker & Couchman 2000; Sommer-Larsen et al. 2003; Brook et al. 2004; Stinson et al. 2006) or a multiphase ISM (Yepes et al. 1997; Hultman & Pharasyn 1999; Marri & White 2003; Scannapieco et al. 2006). In the case of a kinetic feedback, energy is mechanically released (Navarro & White 1993; Springel & Hernquist 2003; Dalla Vecchia & Schaye 2008).

We were very careful to ensure *an accurate budget of gains and losses of energy*, even in the presence of a strong feedback. We also checked that the energy from the supernovae, as predicted by stellar evolution, was fully injected into the galactic system. This particular point is not always granted, especially when using a stochastic implementation of the kinetic feedback (Springel & Hernquist 2003; Dalla Vecchia & Schaye 2008). In practice, at each time step $[t, t + \Delta t]$, we calculate the amount of energy do be released during the explosions of SNe. This quantity $E_{\rm SN}(t)$ is the sum of the contributions of SNeIa and SNeII

$$E_{\rm SN}(t) = \sum_i \Delta E_{i,\rm SN} = \sum_i m_{i,\star,0} \left[n_{i,\rm II}(t)\, E_{\rm II} + n_{i,\rm Ia}(t)\, E_{\rm Ia} \right], \tag{8}$$

where $m_{i,\star,0}$ is the initial mass of the stellar particle i, and $n_{i,\rm II}(t)$ and $n_{i,\rm Ia}(t)$ are the corresponding numbers of SNeII and SNeIa supernovae per unit mass during Δt. The integral of $E_{\rm SN}(t)$ over time is then compared to the energy injected in the system during the feedback procedure.

In the case of kinetic feedback, the particles are pushed away, forming a wind with a velocity on the order of 100 km s^{-1} (Springel & Hernquist 2003; Dalla Vecchia & Schaye 2008). This hardly conserves energy to a satisfactory level. The energy budget is improved if the wind particles are decoupled from the other gas particles or if the dynamical time steps are shortened before the onset of the wind. Unfortunately, this latter solution significantly increases the computation time. Moreover, the choice of a given wind speed limits the amount of energy deposited in each neighboring particle. Hence, the total feedback energy derived from stellar evolution is not always fully transferred, especially in the case of slow winds. Consequently, this technique implicitly leads to the production of strong winds.

For all these reasons, we decided to consider thermal feedback. At each time step, the energy $E_{\rm SN}$ is distributed in thermal form among the surrounding particles using the same weight w_{ij}

as for the distribution of the chemical elements (Eq. (7)). When combined with radiative cooling, this thermal feedback can be inefficient; the radiative cooling of the heated gas becomes very large and the injected energy is instantaneously lost (Katz 1992). In GEAR, the cooling of the gas particle affected by the thermal feedback is switched off for a short adiabatic period of time, t_{ad} (a few Myr) (Gerritsen 1997; Mori et al. 1997; Thacker & Couchman 2000; Sommer-Larsen et al. 2003; Brook et al. 2004; Stinson et al. 2006). As both supernova types release the same amount of energy, the switch is applied to gas particles receiving feedback from both SNeII and SNeIa, without distinction. Thus, the feedback from SNIa may be more effective than the one used by other authors (Stinson et al. 2006, for example). The impact of t_{ad} is discussed in Sect. 5.5. We carefully checked that our implementation of feedback combined with the cooling led to converging results with decreasing time step and increasing resolution.

We did not use any time step limiter to prevent possible numerical problems induced by a pre-shock timestep too long compared to the shock timescale. This time step limiter is important when large differences in temperature occur between the pre- and post-shock media (Saitoh & Makino 2009; Merlin et al. 2010). It is not critical in our case, as the net heating of the ISM caused by SNe explosions never exceeds a factor of 20.

3. Initial conditions

3.1. Evolution of small dark matter halos

We ran a ΛCDM cosmological simulation in order to study the profiles of dark halos with masses between 10^8 and $10^9\,M_\odot$, which are typical of dSphs (Walker et al. 2007; Battaglia et al. 2008). The volume of the simulation is $2^3\,h^{-3}\,\mathrm{Mpc}^3$ and contains 134 217 728 dark matter particles, which results in a particle mass of $4.6 \times 10^3\,M_\odot/h$ and a softening length of 150 pc/h. We took the cosmological parameters from the concordance ΛCDM flat universe based on the Wilkinson microwave anisotropy probe V (WMAP V) data combined with the baryon acoustic oscillations (BAO) in the distribution of galaxies and distances measurements from Type Ia supernova observations (Hinshaw et al. 2009; Komatsu et al. 2009): $\Omega_m = 0.279$, $\Omega_\Lambda = 0.721$ and $h_0 = 0.7$. We extracted the dark halos at different redshifts using the HOP algorithm (Eisenstein & Hut 1998). The halo mass is defined as the mass inside r_{200}, the radius at which the density of matter is 200 times the critical density of the Universe; the halo density profiles have a Navarro-Frenk-White (NFW) shape (Navarro et al. 1996, 1997). We found 144 halos with masses in the range from 10^8 to $10^9\,M_\odot$. The analysis of these halos showed two main features:

(i) for 50% of the halos, the density profiles in *physical* coordinates (as opposed to *comoving* coordinates) are in place at a redshift of 6, i.e., at about 1 Gyr (see Fig. 1). Whilst the Universe was in average about 350 times denser at $z = 6$ than at $z = 0$ (in physical coordinates), the density profiles of the dark halos are similar;
(ii) varying masses by a factor of 10, from 10^8 to $10^9\,M_\odot$, scales the density profiles by a factor of 3–4 only (see Fig. 2).

The consequences for the evolution of dSphs, are (i) the expansion of the universe leads to the formation of stable systems after $z = 6$. This justifies the use of models of dSphs in a static Euclidean space, where the expansion of the universe is neglected. In those models, the physics related to baryons that depends on the density in physical coordinates (for example the cooling of the gas) is correct. This would not be the case if the density in the halos were to increase with the mean density of the universe at higher redshift; (ii) fifty percent of the halos have experienced only minor mergers since $z = 6$. Their profiles are quite relaxed and can be modeled as isolated systems; (iii) although the densities of halos with masses between 10^8 and $10^9\,M_\odot$ are very similar, they exhibit a small dispersion, of a factor from 3 to 4, which can help us to understand the variety in the observed properties of the dSph galaxies.

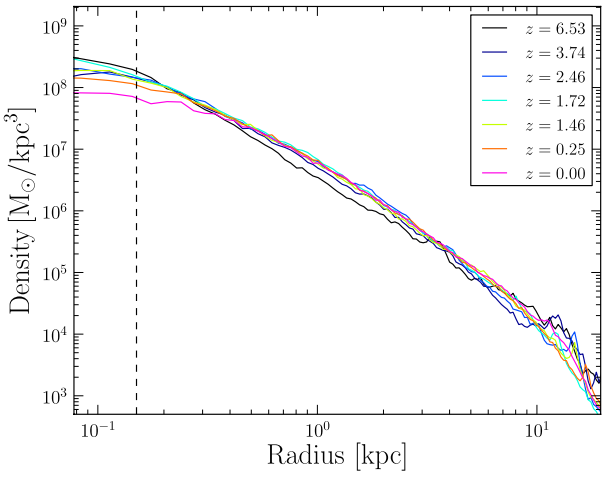

Fig. 1. Evolution of the dark halo density profile for a halo mass of $6 \times 10^8\,M_\odot$ as a function of redshift. The dashed line indicates the limit of the resolution corresponding to the gravitational softening.

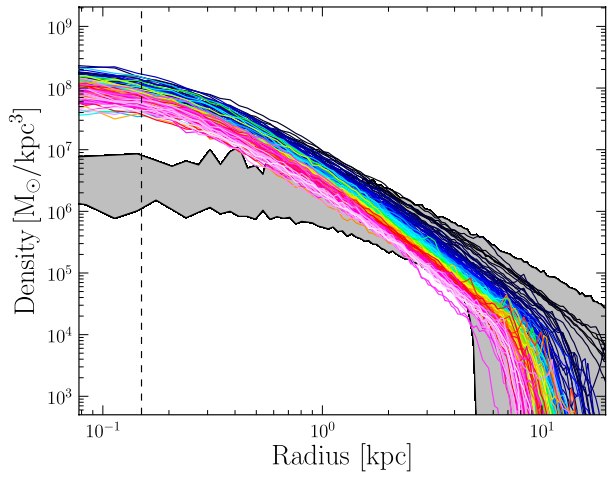

Fig. 2. The density profiles at $z = 0$ of 142 dark matter halos with masses between 10^8 and $10^9\,M_\odot$. The dashed line indicates the limit of the resolution corresponding to the gravitational softening. The gray surface show the domain covered by the pseudo-isothermal profiles (Eq. (9)) adopted in our simulations, for the minimum and maximum values of central densities and radii (r_{max}). Only two halos among the 144 extracted strongly deviate from the NFW profile and are not seen in this plot. The reason is that at $z = 0$, they both undergo a major merging.

3.2. Isolated systems

The previous conclusions warrant the simulation of dSphs as isolated systems, hence our neglect of the expansion of the

Universe. This approach is convenient in terms of CPU time, allowing us to run a large number of simulations to explore a wide range of parameters, as well as to reach very high resolutions.

Our isolated systems are initially spherical and contain dark matter as well as 15% of their baryons in the form of gas. To a first approximation, we assume the same profile for the gas and the dark matter.

Instead of using an NFW profile, we decided to use a cored one, which is supported by observations of normal low brightness and dwarf galaxies (Blais-Ouellette et al. 2001; de Blok & Bosma 2002; Swaters et al. 2003; Gentile et al. 2004, 2005; Spekkens et al. 2005; de Blok 2005; de Blok et al. 2008; Spano et al. 2008; Walker & Peñarrubia 2011), including the recent and high resolution observations of the THINGS survey (Oh et al. 2011). Both gas and dark matter follow a pseudo-isothermal profile

$$\rho_i(r) = \frac{\rho_{\rm c,i}}{1 + \left(\frac{r}{r_{\rm c}}\right)^2}, \tag{9}$$

where r is the radius, $r_{\rm c}$ is the scale length of the mass distribution, and $\rho_{{\rm c},i}$ is the central mass density of the component i.

All parameters are set to provide profiles that are compatible with the ΛCDM cosmological simulation discussed above, except in the central regions, where the profiles are flattened (see the gray area of Fig. 2).

Both the initial dark matter and gas profiles are truncated at $r_{\rm max}$ and the total initial mass is then defined as

$$M_{\rm tot} = 4\pi\rho_{\rm c,tot}\, r_{\rm c}^3 \left[\frac{r_{\rm max}}{r_{\rm c}} - \arctan\left(\frac{r_{\rm max}}{r_{\rm c}}\right)\right], \tag{10}$$

where $\rho_{\rm c,tot} = \rho_{\rm c,halo} + \rho_{\rm c,gas}$.

As the precise value of $r_{\rm c}$ has only a limited influence on the evolution of the dSphs (Revaz et al. 2009), we fixed it to be 1 kpc, where $\rho_{\rm c,halo}$ and $\rho_{\rm c,gas}$ are related by the baryonic fraction.

In the case of spherical systems and for an isotropic velocity dispersion, the velocities of a component i can be derived using the second moment of the Jeans equation (Binney & Tremaine 1987; Hernquist 1993):

$$\sigma_i^2(r) = \frac{1}{\rho_i(r)} \int_r^\infty {\rm d}r'\, \rho_i(r')\, \partial_{r'}\Phi(r'). \tag{11}$$

For the halo, the velocity dispersion is directly taken from Eq. (11). For the gas, the initial velocities are set to zero but its initial temperature is obtained by converting the kinetic energy of Eq. (11) into thermal energy:

$$T(r) = f_{\rm vir}(\gamma - 1)\frac{\mu {\rm m_H}}{k_{\rm B}}\frac{3}{2}\sigma^2_{\rm gas}(r), \tag{12}$$

the parameter $f_{\rm vir}$ set to 0.5 allows the gas to slowly flow towards the center of the system, where $\rm m_H$ is the hydrogen mass, μ, the mean atomic mass of the gas and $k_{\rm B}$ the Boltzman constant.

4. Robustness

4.1. Energy conservation

The first and fundamental requirement of numerical simulations is to carefully trace all sources (gain and loss) of energy in the systems: the total potential energy, the total kinetic energy, the gas internal energy, the radiative cooling energy, and the SNe feedback energy. We also include in the gas internal energy, the internal energy of gas particles converted into stars. The precision of our energy budget is always better than 5%. As an example, Fig. 3 displays the global budget of the energy of a massive 9.5×10^8 $M_\odot$ system, with $c_\star = 0.05$ and $\epsilon_{\rm SN} = 0.03$, $\rho_{\rm c,gas} = 0.071\,{\rm m_H/cm^3}$. The total number of particles is 524 288 and the softening length 25 pc. Such a high mass system, with a high central mass density, experiences sustained star formation at a high level (see Sect. 7), making it a difficult case from a numerical point of view. Nevertheless, the energy is conserved to within 5%. This is remarkable with regards to the long integration time (14 Gyr) relative to the dynamical time of the system (about 50 Myr). Figure 3 also reveals a clear balance between the injected energy by the SNe explosions and the radiative cooling. This means that although the cooling is switched off during an adiabatic period $t_{\rm ad}$ (see Sect. 2.4), a large fraction of the feedback energy is still radiated away.

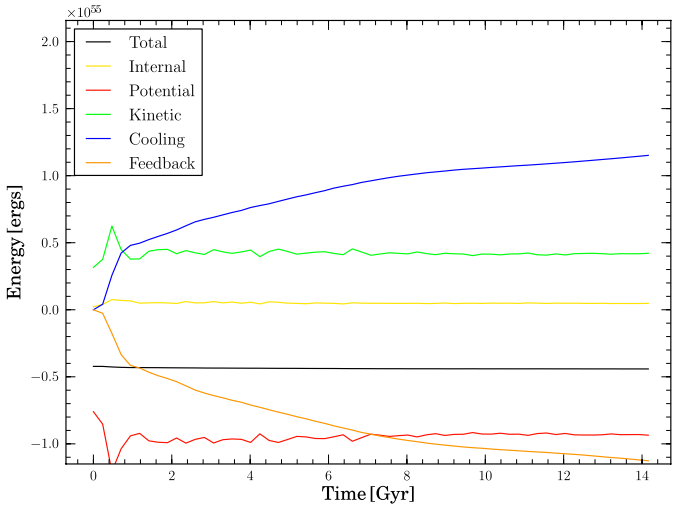

Fig. 3. Global energy budget for a dense and massive model of 9.5×10^8 $M_\odot$ ($\rho_{\rm c,gas} = 0.071{\rm m_H/cm^3}$, $c_\star = 0.05$ and $\epsilon_{\rm SN} = 0.03$) as a function of time. The total energy (in black) is the sum of all other lines, namely: the total potential energy (in red), the total kinetic energy (in green), the gas plus stellar internal energy (in yellow), the radiative cooling energy (in blue), and the SNe feedback energy (in orange). The latter is negative because it corresponds to energy injected into the system.

4.2. Convergence

We verified that we could achieve convergence of our results with increasing resolution, i.e., the number of particles was increased and the gravitational softening $\epsilon_{\rm g}$ was decreased accordingly. For this, we performed eight sets of simulations on systems with two different masses, 3 and 9.5×10^8 $M_\odot$, exploring both weak ($\epsilon_{\rm SN} = 0.03$) and strong ($\epsilon_{\rm SN} = 1$) feedback. The sizes of the systems were the same and their central gas density were, respectively, $\rho_{\rm c,gas} = 0.025$ and $\rho_{\rm c,gas} = 0.066\,{\rm m_H/cm^3}$.

The initial number of particles was increased from $2^{13} = 8092$ to $2^{22} = 4\,194\,304$, corresponding to a mass resolution of about 10^4 $M_\odot$ and 20 $M_\odot$, respectively. This is equivalent to changing the mass resolution by a factor of 512, and the spatial resolution by a factor of eight. We start by discussing the case of the weak feedback. The main properties of the simulations are summarized in Table 1, where in all cases $c_\star = 0.05$ and $f_{\rm vir} = 0.25$. Figure 4 displays the evolution of the star formation rates and the corresponding increases in stellar mass. The quantity of stars formed results from the complex interplay between

Table 1. Properties of the runs performed for the convergence tests.

$M_{\rm tot}$ [$10^8\ M_\odot$]	$\rho_{\rm c,gas}$ [m_H/cm^3]	N	$m_{\rm gas}$ [$M_\odot$]	$\epsilon_{\rm g}$ [pc]
9.5	0.071	2^{13} = 8′192	3.16×10^4	100
–	–	2^{16} = 65′536	4.11×10^3	50
–	–	2^{19} = 524′288	5.00×10^2	25
–	–	2^{22} = 4′194′304	6.17×10^1	12.5
3.0	0.022	2^{13} = 8′192	1×10^4	100
–	–	2^{16} = 65′536	1.3×10^3	50
–	–	2^{19} = 524′288	1.58×10^2	25
–	–	2^{22} = 4′194′304	1.95×10^1	12.5

Notes. $M_{\rm tot}$ is the initial total mass of the system, $\rho_{\rm c,gas}$ is the initial central gas density, N is the initial total number of particles (gas and dark matter) and $\epsilon_{\rm g}$ is the gravitational softening. These models were run with $c_\star = 0.05$ and $\epsilon_{\rm SN} = 0.03$.

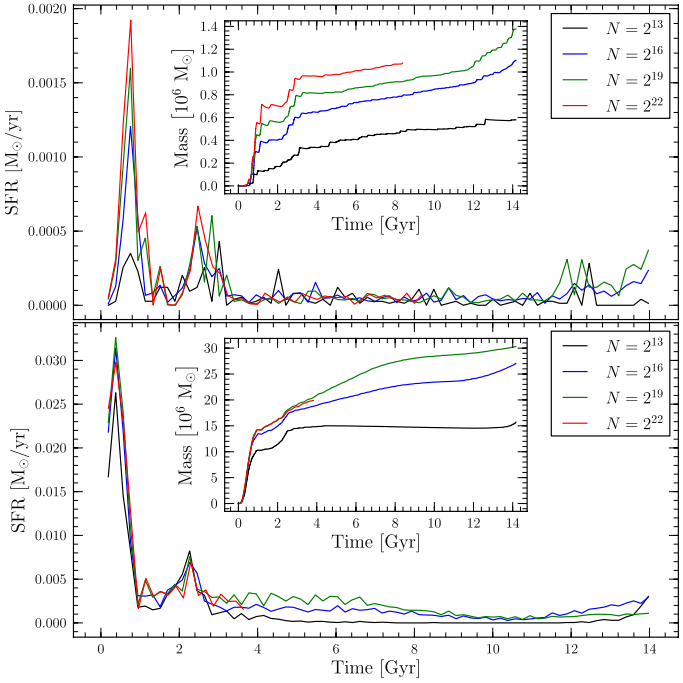

Fig. 4. Star formation rate and stellar mass as a function of time for the two models of Table 1. Each line corresponds to a different resolution.

the gas cooling and feedback heating and thus closely follows all the implemented physical processes. Figure 4 shows that changing the resolution does not alter the position of the peaks of star formation which remain at the same epochs. High resolutions models form two to five times more stars over a longer period than the low resolution ones. This is the consequence of an improved sampling of the high central density peaks, which translates into shorter cooling times.

The impact of a change in numerical resolution is slightly larger for low mass systems than for massive ones. The two simulations with 4 194 304 particles are still running at the time of writing this paper hence their corresponding red curves are still incomplete. However, during the first 4 Gyr, the star formation history of the $9.5 \times 10^8\ M_\odot$ model is similar for the simulations with the $N = 2^{19}$ and $N = 2^{22}$ resolutions. In the case of the lower mass system, the difference in stellar mass between the $N = 2^{19}$ and $N = 2^{16}$ models is on the order of 15% during the 8 first Gyr. This increase in mass is nevertheless moderate and does not translate into different star formation histories, hence

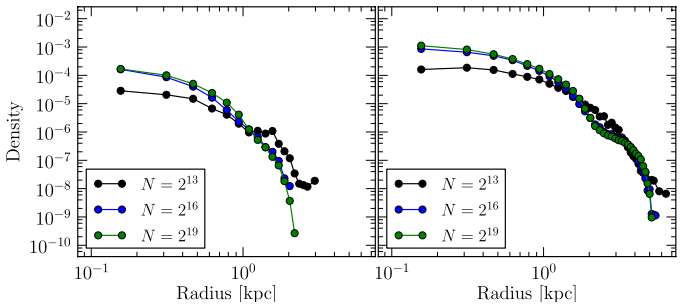

Fig. 5. Stellar density profiles for the models of mass 3 (*left*) and $9.5 \times 10^8\ M_\odot$ (*right*) described in Table 1 with different resolutions, at t = 14 Gyr.

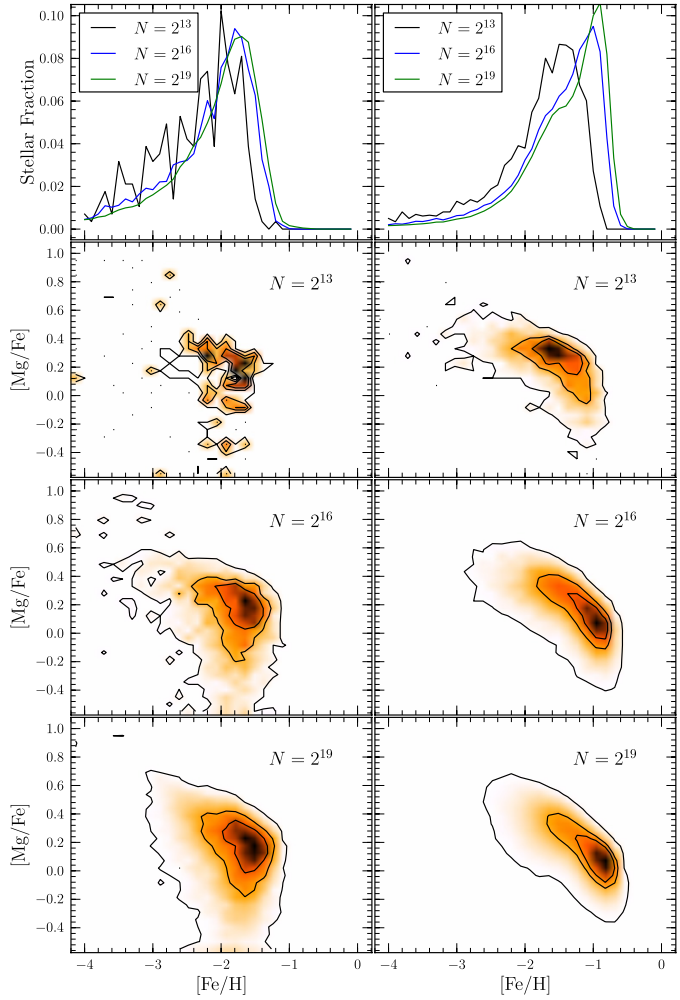

Fig. 6. [Fe/H] distributions and [Mg/Fe] vs. [Fe/H] diagrams at t = 14 Gyr for the two models described in Table 1. The galaxy with a mass of $3 \times 10^8\ M_\odot$ is shown on the left column, while the model with $9.5 \times 10^8\ M_\odot$ is displayed on the right column.

different age or metallicity distributions and chemical abundance patterns.

Figure 5 shows the stellar profiles, which depend directly on the dynamics. They show that a low spatial resolution leads to flatter profiles than at higher resolution.

Figure 6 indeed, illustrates how the metallicity distributions and abundance ratios are sensitive to the resolution. A low resolution ($N < 2^{13}$) tends to artificially shift the metallicity

distribution to lower values and provide an incomplete view of the chemical evolution. A satisfactory level of convergence is again obtained for $N = 2^{16}$ particles, leading to [Fe/H] differences of less than 0.1 dex.

We performed the same tests for a strong feedback ($\epsilon_{SN} = 1$) and could verify that convergence is also achieved. This is remarkable because such an extreme feedback inhibits star formation. Consequently, only a small number of stellar particles form that in turn may lead to a high noise level as star formation is implemented as a stochastic process.

In summary, our tests demonstrate the reliability of the numerical implementation of the physical processes described in Sect. 2, which are independent of the number of particles used. Above a resolution of $N = 2^{16}$ particles, the physical quantities are described with sufficient accuracy. The convergence arises from the balance between feedback and cooling; our systems are self-regulated. In the rest of this paper, we use $N = 2^{16}$, a good trade-off between resolution and CPU time.

4.3. Random number seed

Whilst convergence of our results is obtained, our system may nevertheless still be nonlinear at fixed resolution owing to the complexity of the physics. For example, changing the cooling affects the star formation, which in turn impacts the feedback and the cooling again, etc. The integration time of 14 Gyr is long relative to the dynamical times of the galaxies which is on the order of 50 Myr. Small perturbations might produce a large dispersion in the final properties of the galaxies. In the following, we investigate this issue and evaluate the error bars attached to our outputs. Random numbers are used by the star formation algorithm and can act as perturbations. Therefore, we performed three different sets of simulations, in which only the random number seed was modified. The left part of Table 2 summarizes the parameters of our simulations.

Figure B.1 displays the case of model #1111, which presents the largest deviations. They are anyway very small. Even after several dynamical times of evolution, the system is not strongly affected by the perturbations generated by the use of a different random number sequence.

Table 2 quantifies the relative variations in stellar mass, V-band luminosity, and final mode metallicity. These variations are estimated as the ratio of the absolute difference between the minimum to the maximum of the measured quantity divided by its mean value. The final stellar masses deviate by ~6% at most and the metallicities by 11%, while the luminosities can vary by 26%, owing to the strong dependence of the luminosity on the stellar age. These values can be interpreted as the error bars intrinsic to the models. They must be kept in mind when comparing models with observations.

5. Parametrization

Physical processes involved in galaxy formation, such as star formation, feedback, or cooling occur typically on length and time scales much smaller than the ones resolved by current numerical simulations. As described in Sect. 2, these sub-grid processes are modeled using phenomenological prescriptions and require the introduction of a set of parameters. Table 3 compiles the list of our model parameters, and following we explore their role. Unless specified otherwise, the discussions are based on the full set of 393 simulations.

5.1. Feedback efficiency ϵ_{SN}

The feedback efficiency, ϵ_{SN}, is the fraction of energy released by the explosion of supernovae, which is effectively deposited into the interstellar medium. The remaining fraction is assumed to be radiated away, without impacting the system. Our feedback prescription is thermal (see Sect. 2.4), hence it modifies the temperature, the pressure, and consequently the density of the gas surrounding the exploding stellar particles and in turn impacts the eligibility of the gas particles to form stars. Figure 7 displays the final mode stellar metallicity [Fe/H] and V-band luminosity (L_v) as a function of the initial total mass of the system.

If 100% of the supernova energy is injected in the ISM ($\epsilon_{SN} = 1$, open circles in Fig. 7), the final mode metallicity of the system is always below the values measured for the Local Group dSphs and UFDs (red vertical line). Similarly, the luminosities are generally very low. For such high values of ϵ_{SN}, the feedback energy is maximal and strongly heats and dilutes the ISM pushing the gas particles away from the criteria for star formation, which is stopped. The subsequent increase in the cooling time, mainly driven by the decrease in the gas density, is so strong that it inhibits any star formation during the rest of the galaxy evolution.

It is clear that ϵ_{SN} must be decreased below 1 in order to reach metallicities and luminosities compatible with the observations. Figure 7 presents our result for ϵ_{SN} in the range 0.1 to 0.01. In addition, it shows that the initial total mass of the systems drives the final luminosity and metallicities, and that ϵ_{SN} primarily influences the least massive systems. At very low ϵ_{SN}, the cooling of the gas is no longer counterbalanced by the supernova feedback: stars can form efficiently and longer, leading to high metallicities. Figures B.2 and B.3 also illustrate how the ISM becomes more homogeneous with decreasing ϵ_{SN}, diminishing the dispersion in stellar abundance ratios. To constrain ϵ_{SN}, keeping its value fixed for all galaxies, we need to consider the full set of dSph properties. Our generic models (see Sect. 7.2) are obtained with $\epsilon_{SN} = 0.03$.

5.2. Threshold density for star formation ρ_{sfr}

A threshold density for star formation, ρ_{sfr}, was introduced in a cosmological context by Summers (1984) to avoid the formation of stars in low density regions. The value of 0.1 m_H/cm^3, that is widely used in the literature (e.g., Alimi et al. 2003; Stinson et al. 2006; Valcke et al. 2008), was introduced by Katz et al. (1996) and corresponds to the mean density of the warm neutral medium of our galaxy. Since ρ_{sfr} fixes the local density at which stars are allowed to form, it may as well influence the global galaxy star formation history.

The importance of this threshold density was discussed in the context of disk galaxies (Tasker & Bryan 2006, 2008). Saitoh et al. (2008) concluded that only models using a high threshold density ($\rho_{sfr} = 100\ m_H/cm^3$) are able to reproduce the complex, inhomogeneous, and multiphase structure of the ISM. Hereafter, we investigate the consequences of varying the critical density in the context of dSph galaxies.

For $c_\star = 0.05$ and $\epsilon_{SN} = 0.05$, we varied ρ_{sfr} from 0.05 to 100 m_H/cm^3 for two different initial masses, 3.5 and $7 \times 10^8\ M_\odot$, within $r_{max} = 8$ kpc and the initial central gas densities of 0.025 and 0.053 m_H/cm^3, respectively. A zoom on the first few Gyr evolution of the star formation rate and stellar mass of the $3.5 \times 10^8\ M_\odot$ model is provided in Fig. 8. It shows that the increase in ρ_{sfr} imposes an increasing delay on the onset of the star formation, because the gas needs to become gradually denser.

Table 2. Properties of the models for which the random number seed was modified.

Model	$M_{\rm tot}$ [$10^8\,M_\odot$]	$\rho_{\rm c,gas}$ [$\rm m_H/cm^3$]	$c_\star$	$\epsilon_{\rm SN}$	$\delta(M_\odot)$ [%]	$\delta(L_{\rm v})$ [%]	δ([Fe/H]) [%]
885	3	0.022	0.05	0.03	4	9	11
1111	8	0.029	0.1	0.05	6	26	6
1056	7	0.059	0.03	0.03	3	13	0

Table 3. List of model parameters.

Context	Quantity	Symbol	Reference values	Variation
initial conditions	baryonic fraction	$f_{\rm b}$	0.15	no
	dark halo core radius	$r_{\rm c}$	1 kpc	no
	virial fraction	$f_{\rm vir}$	0.5	no
	total mass	$M_{\rm tot}$	-	$[1–9\times10^8\,M_\odot]$
	gas central density	$\rho_{\rm c,tot}$	-	$[0.005–0.063\ \rm m_H/cm^3]$
	initial outer radius	$r_{\rm max}$	-	[1.91–24.4 kpc]
gravity	softening	$\epsilon_{\rm g}$	50 pc	[adaptive]
sph	number of neighbors	$N_{\rm ngb}$	50	[50, 100]
cooling	cooling function	Λ	Sutherland & Dopita (1993); Maio et al. (2007)	no
star formation	parameter	$c_\star$	0.05	[0.01–1]
	critical density	$\rho_{\rm sfr}$	$0.1\ \rm m_H/cm^3$	$[0.05–100\ \rm m_H/cm^3]$
	maximal number of stellar particles per gas particle	$N_\star$	4	[1–15]
	gas temperature	$T_\star$	3×10^4 K	no
stellar evolution	initial mass function	IMF	Kroupa (2001)	[Kroupa, Salpeter]
	yields	-	Iwamoto et al. (1999); Tsujimoto et al. (1995)	no
thermal feedback	supernova energy	$E_{\rm SN}$	10^{51} erg	no
	efficiency	$\epsilon_{\rm SN}$	0.03	[0.01–1]
	adiabatic period	$t_{\rm ad}$	5 Myr	[2–30 Myr]

Notes. The reference values indicate our final set of adopted parameters based on the four generic models of Local Group dSphs. The last column indicates whether or not the parameters were varied (see Sects. 5 and 6), in which case we give their range of values.

Moreover, one passes from a regime of large and moderately intense peaks of star formation to a series of higher intensity and higher frequency episodes, creating a larger number of stars, although varying $\rho_{\rm sfr}$ by a factor 1000 does not change the final stellar mass by more than a factor 2.5. Drastic changes in the metallicity distributions and abundance ratios can be seen in Fig. B.8.

Following the course of the formation of the galaxies, it is clearly evident that for low $\rho_{\rm sfr}$ ($<1\ \rm m_H/cm^3$), the first generations of stars form within a relatively large region (radius ~300 pc), roughly corresponding to the SPH sphere (radius ~250 pc) in these low density medium. Metals and energy feedback are homogeneously distributed. For higher star formation density thresholds, the evolution of the systems is quite different. Because the density of the gas is higher, the size of the star forming region is smaller, with typical radii on the order of ~30 pc for $100\ \rm m_H/cm^3$, again corresponding roughly to the SPH sphere radius (~15 pc). Since the mechanisms of metal ejection and energy feedback are described by the SPH formalism, metals are distributed very locally. The release of the energy of the supernova explosions creates bubbles, which inflate and push back the surrounding gas significantly increasing its density. The rims of the gas bubbles are dense enough to cool quickly. They become unstable and form stars. In this way, star formation induces further star formation. This explains the increase in stellar mass at high $\rho_{\rm sfr}$, observed in the bottom of Fig. 8.

The metallicity distributions and abundances ratios generated by $\rho_{\rm sfr} > 1\ \rm m_H/cm^3$ look incompatible with the observed galaxy properties and are consequently discarded. We thus keep the value of 0.1, which satisfies the abundances constraints most closely.

5.3. Star formation parameter $c_\star$

The star formation parameter $c_\star$ is a dimensionless parameter that controls the number of stars formed from the gas. In the context of spiral galaxies, $c_\star$ may be calibrated using a Kennicutt-Schmidt law (Schmidt 1959; Kennicutt 1998). Unfortunately, as dSphs are devoid of gas, no similar relation exists for them. The impact of the variation in $c_\star$ has been discussed by Stinson et al. (2006) in the context of their feedback blast wave model. Their mean star formation rate varies by only a factor ~1.2 when $c_\star$ goes from 0.05 to 1.

We performed a similar study for our pressure-supported systems, varying $c_\star$ by two dex, from 0.01 to 1. We considered two models with $3.5\times10^8\ M_\odot$ ($\rho_{\rm c,gas} = 0.025\ \rm m_H/cm^3$, $\epsilon_{\rm SN} = 0.05$) and $7\times10^8\ M_\odot$ ($\rho_{\rm c,gas} = 0.053\ \rm m_H/cm^3$, $\epsilon_{\rm SN} = 0.05$). The comparison of the galaxy final state is provided in Figs. B.6 and B.7. Figure 9 presents a zoomed image of the first few Gyr of evolution for the $3.5\times10^8\ M_\odot$ model. Independently of the mass of the dSph, a large $c_\star$ results in a very discontinuous star formation history. This is a direct consequence of the coupling

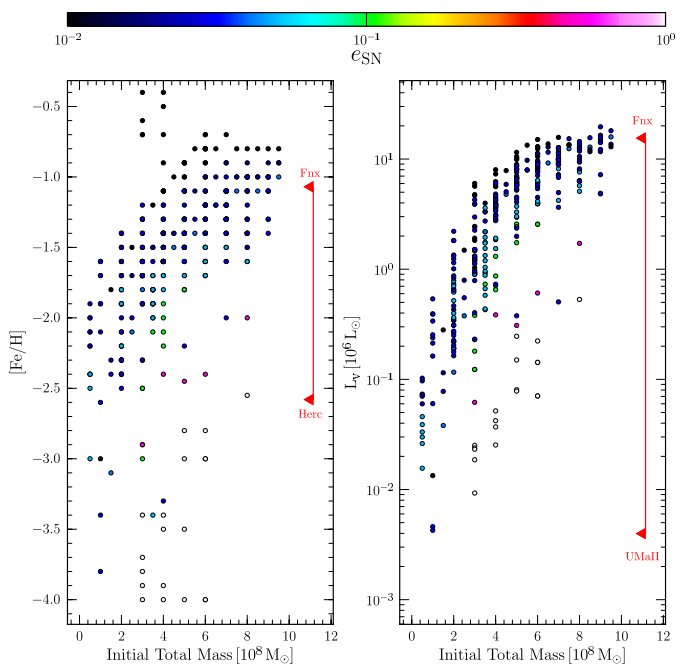

Fig. 7. Final [Fe/H] and luminosity L_v as a function of the total initial mass of the system. Our full set of simulations is shown. The colors code the supernova feedback efficiency, between 0.01 and 1. In each panel, a red line indicate the range of metallicity or luminosity covered by the Local Group dSphs.

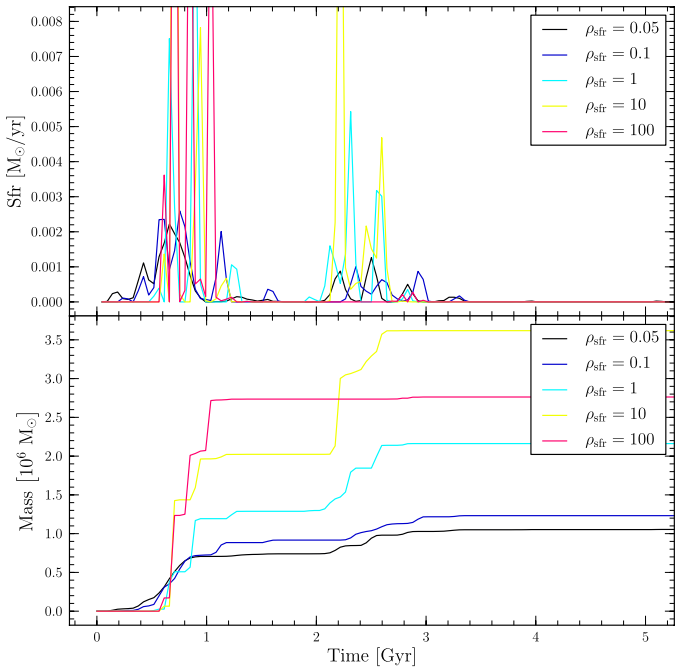

Fig. 8. The effect of varying ρ_{sfr}. This figure illustrates the case of a 3.5×10^8 $M_\odot$ mass system, with an initial gas density of 0.025 m$_H$/cm^3. The *upper panel* shows the evolution of the star formation rate with time, while the *lower panel* displays how mass increases.

between star formation and feedback. In the extreme case of $c_\star = 1$ and $M_{tot} = 3.5 \times 10^8$ $M_\odot$, 99% of the stars are formed during a first burst. This dramatically impacts the metallicity distribution and metal abundances (see Fig. B.6). Metal-poor stars ([Fe/H] < -2.5) with high [Mg/Fe] ~ 1 are dominant. These

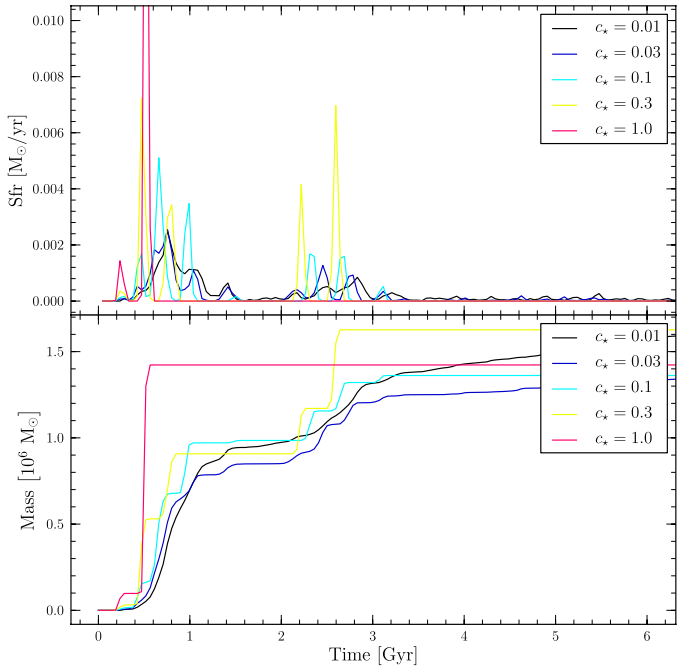

Fig. 9. Star formation rate and stellar mass as a function of time for models of mass 3.5×10^8 $M_\odot$ ($\rho_{c,gas} = 0.025$ m$_H$/cm^3) with different $c_\star$.

systems are unrealistic. The long period of quiescence following the first and dominant peak results from an important physical process, which is discussed in Sect. 7.1.

In contrast, at lower $c_\star$ the galaxy experiences a more continuous star formation history, resulting from a better self-regulation between cooling and heating. The moderate intensity of the initial bursts allows the gas to cool. This gives rise to the presence of intermediate age stellar populations and higher mean metallicity.

The full evolution of the stellar mass with time is displayed in Figs. B.6 and B.7. Differences in the final stellar masses remain smaller than 50%. Increasing $c_\star$ slightly decreases the quantity of stars formed. This counterintuitive result is also found by Stinson et al. (2006) at large $c_\star$. A model with a higher $c_\star$ quickly forms a large number of stars. The feedback energy due to the SNeII explosions is released nearly instantaneously. The gas is blown out and the star formation is quenched. At later times, the large number of SNeIa continue to prevent star formation, as discussed in more detail in Sect. 7.1.

5.4. Number of stellar particles $N_\star$ created from a gas particle

The mass of the stellar particles $m_\star$ is linked to the mass of the gas particles m_g via the parameter $N_\star = m_g/m_\star$. It can also be seen as the maximum number of stellar particles that can be created per gas particle in the absence of gas accretion. In principle, Eq. (4) regulates the impact of the mass resolution of the simulations, leading to the same integrated star formation rate. Nevertheless, this is not fully the case once cooling and feedback are taken into account. Augmenting $N_\star$ increases the sampling of the star formation. A small number of big particles are replaced by a larger number of smaller ones, distributed along the same period of time, and for an equal final stellar mass. The price to pay is obviously a large increase in the CPU time needed for

a simulation. According to Springel & Hernquist (2003), a good compromise between time resolution and CPU saving is $N_\star = 4$.

We varied $N_\star$ between 1 and 15 for a $5 \times 10^8\,M_\odot$ ($r_{\rm max}$ = 8 kpc, $\rho_{\rm c,gas} = 0.037\,{\rm m_H/cm^3}$, $c_\star = 0.025$, $\epsilon_{\rm SN} = 0.02$). The results are displayed in Fig. B.10. Two effects are observed.

The final metallicity mode of the systems decreases within larger $N_\star$, by a factor of two passing from $N_\star = 1$ to 15. A large number of small stellar particles regularly inject feedback energy into the interstellar medium, preventing it cooling and being able to host star formation again. In contrast, as the probability of forming stars for large $N_\star$ is low, the system is slightly cooler and denser when the first stars form, leading to a higher star formation peak. Whilst the mean metallicity of the systems are similar within 0.3 dex, a clear trend is observed in the abundance ratios. The dispersion in [Mg/Fe] is significantly smaller for higher $N_\star$ (high chemical mixing), again owing to the frequent feedback of the numerous stellar particles, starting early in the evolution of the galaxies.

Small abundance dispersions at low metallicities are the rule in observed galaxies. This favors high $N_\star$. The dispersion does not increase substantially between $N_\star = 4$ and $N_\star = 15$ (see Fig. B.10), therefore saving CPU time, we set it to 4.

5.5. Supernova adiabatic period $t_{\rm ad}$

The adiabatic period $t_{\rm ad}$ fixes the period of time during which the cooling of the gas particles that have received the thermal supernova feedback, is stopped. As discussed in Sect. 2.4, this period improves the feedback efficiency by avoiding the instantaneous loss of energy by radiative cooling. The time $t_{\rm ad}$ must be much longer than the dynamical time steps, which is at most 0.2 Myr in our case as imposed by the resolution of the chemical evolution (see Sect. 2.3), to ensure the convergence of the simulation. It is often set to 30 Myr, the longest lifetime of the least massive SNII progenitor ($8\,M_\odot$). Stinson et al. (2006) proposed a new feedback recipe based on an analytical treatment of supernova blast-waves. In this model, $t_{\rm ad}$ depends on the local gas density and pressure.

We explored the effect of $t_{\rm ad}$, between 2 Myr and 30 Myr, for two models, $M_{\rm tot} = 3.5$ ($r_{\rm max}$ = 8 kpc, $\rho_{\rm c,gas} = 0.025\,{\rm m_H/cm^3}$) and $7 \times 10^8\,M_\odot$ ($r_{\rm max}$ = 8 kpc, $\rho_{\rm c,gas} = 0.051\,{\rm m_H/cm^3}$). Both models have $c_\star = 0.05$ and $\epsilon_{\rm SN} = 0.05$. The results are displayed in Figs. B.4 and B.5. Increasing $t_{\rm ad}$ decreases the final stellar mass in both cases. This is the consequence of a reduction in cooling. However, the effect remains weak. After 14 Gyr, the amount of stellar mass formed is diminished by a factor of from 1.3 to 1.6. This is insufficient to change substantially the chemical properties of the final dwarf galaxy. In the following, we fix $t_{\rm ad}$ to 5 Myr.

5.6. Number of particles in a softening radius $N_{\rm ngb}$

As described in Sects. 2.3 and 2.4, the stellar ejecta as well as the feedback energy are spread in the SPH sphere. Increasing the size of the SPH sphere, i.e., increasing the number of neighbors when computing the local physical quantities, allows us to distribute metals to larger radii.

In galaxy cluster simulations, Tornatore et al. (2007) varied $N_{\rm ngb}$ from 16 to 128. They reported only marginal differences, although increasing the number of neighbors produced somewhat higher star formation rates, presumably owing to the large number of particles affected by metal-line cooling.

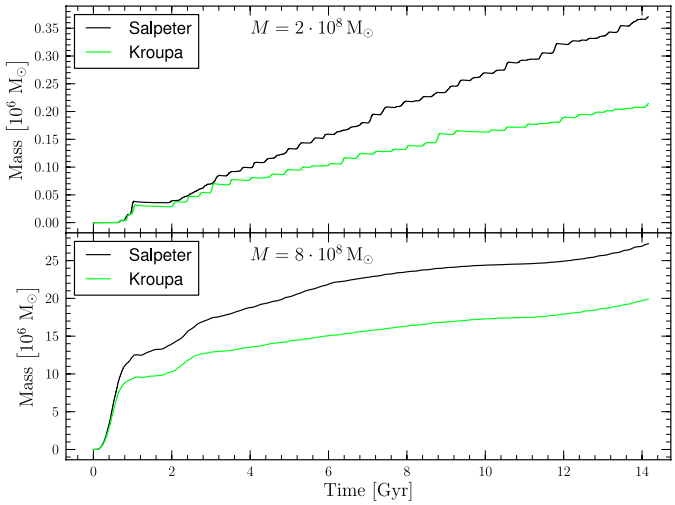

Fig. 10. The difference in stellar mass growth with time when changing of IMF. Two examples are shown, at $2{\times}10^8\,M_\odot$ ($\rho_{\rm c,gas} = 0.015\,{\rm m_H/cm^3}$) and $8\,\times 10^8\,M_\odot$ ($\rho_{\rm c,gas} = 0.053\,{\rm m_H/cm^3}$).

We performed a similar test with a $4 \times 10^8\,M_\odot$ ($r_{\rm max}$ = 8 kpc, $\rho_{\rm c,gas} = 0.029\,{\rm m_H/cm^3}$) simulation, and changing $N_{\rm ngb}$ from 50 to 100. The final state of the systems are displayed in Fig. B.13. The difference between the two models is very small, in agreement with Tornatore et al. (2007). However, we reach an opposite conclusion. After doubling $N_{\rm ngb}$, the final stellar content becomes slightly lower (factor 1.33). This induces a slight decrease in the mean metallicity (<0.1 dex). The reason is probably linked to the different treatment of the feedback in the two studies. The model of Tornatore et al. (2007) is based on the wind scheme of Springel & Hernquist (2003).

5.7. The IMF

We finally checked the impact of the choice of IMF on our results. For this, we used the classical Salpeter IMF (Salpeter 1955), defined by a constant slope of −2.35. The Kroupa (2001) IMF contains fewer stars with masses lower than $0.2\,M_\odot$ than the Salpeter's one. As a consequence of normalization, this means more stars in the mass range of supernovae ($>8\,M_\odot$) by a factor 1.5, and thus more feedback energy. Figure 10 illustrates that fewer stars are formed with a Kroupa IMF than with a Salpeter one.

This weak difference in the final stellar mass does not have a substantial impact on either the metallicity distributions or the [Mg/Fe] abundance ratios (see Figs. B.11 and B.12).

6. Mass and central density

In the previous section, we explored the role of the parameters inherent to GEAR. We now discuss the effects of changes in the initial total mass of the galaxy and the initial central gas density, which are linked to the initial conditions.

Revaz et al. (2009) found that the galaxy total initial mass estimated within a fixed radius is an important parameter, that can determine both the final metallicity and the luminosity of the galaxies. We confirm this result as illustrated in Fig. 7, which can be compared with Fig. 5 of Revaz et al. (2009).

As described in Sect. 3.1, the dark matter profiles derived from the ΛCDM simulations exhibit a small dispersion in their

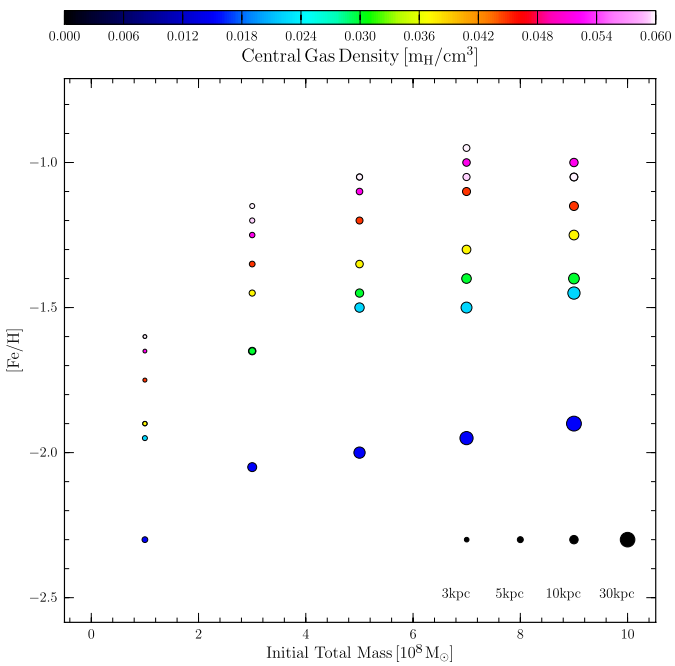

Fig. 11. Final mode [Fe/H] as a function of the total initial mass of the system. The size of the circles scales with the initial size (radius) of the system, as featured at the bottom right of the figure. The color code the initial gas density. For all models $c_\star = 0.05$ and $\epsilon_{SN} = 0.03$.

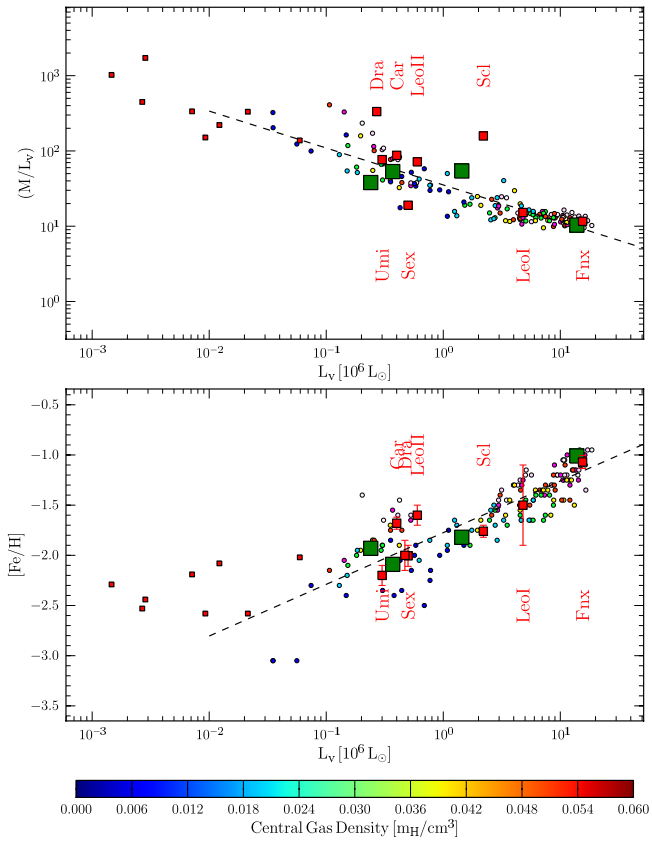

Fig. 12. Global relations. The galaxy mass-to-light ratios, M/L_v (*top panel*) and the mode of their final metallicity distributions (*bottom panel*), versus their V-band luminosities L_V. Each circle stands for one of our 160 models, with $c_\star$ and ϵ_{SN} restricted to the intervals 0.05–0.1 and 0.03–0.05, respectively. The central gas density and total mass range is 0.005–0.06 m_H/cm^3 and $1–9 \times 10^8$ $M_\odot$. Colors code the initial central gas density. The red large squares represent the Local Group classical dSphs, while the smallest red squares represent the ultra faint dwarfs. The dashed lines correspond to our best model fit. The green squares indicate the position of our selected generic models, from left to right, Carina, Sextans, Sculptor, and Fornax.

central regions, which should be investigated. Indeed, the initial gas profile follows the dark matter one in our models, and the gas density determines the cooling time. Moreover, the star formation criterion involves a threshold in gas density. All these facts motivated us to examine the role played by the central density in addition to that of the total mass. Carraro et al. (2001) recovered different star formation histories for objects of the same total mass when their collapse phase started at different initial densities.

At a given central density ($\rho_{c,gas}$), the total mass (M_{tot}) of the system can be varied by increasing/decreasing its size with r_{max}. Similarly, for a given total mass, the central density can be varied increasing/decreasing its size with r_{max}. Figure 11 presents the variation in the final mode metallicity as a function of the initial mass and the central gas density. We present 40 simulations, all with $c_\star = 0.05$ and $\epsilon_{SN} = 0.03$, where $\rho_{c,gas}$ is varied from 0.007 up to 0.063 m_H/cm^3 and M_{tot} from 1 to 9×10^8 $M_\odot$. Consequently, the outer galaxy radius varies between 1.8 and 25 kpc.

For the range of metallicities covered by the Local Group dSphs, an increase in the mass by a factor of ten, at fixed central density, increases the final metallicity of the system by only a few tenths of dex. The largest variation is obtained for very small systems of mass from 10^8 $M_\odot$ to 3×10^8 $M_\odot$, the mode metallicity can increase by 0.4 dex at fixed density; above 3×10^8 $M_\odot$, variations soften until they are essentially indiscernible. Above 3×10^8 $M_\odot$, the additional amount of matter provided by the extension of the system (increase in r_{max}) does not strongly affect its final chemical properties (metallicity distribution and [Mg/Fe] vs. [Fe/H]). It acts primarily on enhancing the final total stellar mass, while slightly modifying the age distribution of the stellar population. This latter consequence is mainly seen at low densities ($\rho_{c,gas} \sim 0.015$ m_H/cm^3). These points are also illustrated in Figs. B.14 and B.15, with different $c_\star$ and ϵ_{SN} than in Fig. 11.

In contrast, a variation by a factor 10 in the central gas density can vary the final metallicity by more than a dex, making it the primary driving parameter. The cooling time is shorter for larger densities, enhancing the star formation, and therefore resulting in more luminous and metal-rich systems. At high enough central densities, all models, even the least massive ones, may experience a strong initial burst, as seen in Fig. B.16. In the range $\rho_{c,gas} = 0.015$ to 0.037 m_H/cm^3, the star formation history can be fully modified. An example is provided in Fig. B.17, where the central density is varied by a factor of four, passing from a low and continuous star formation to a strong initial burst.

7. The different observed regimes of star formation

Figure 12 presents [Fe/H] and M/L vs. luminosity plots for the full series of simulations, which are globally compatible with the observations. This represents a total number of 160 simulations with $c_\star$ in the range 0.05–0.1, ϵ_{SN} of 0.03–0.05, $\rho_{c,gas}$ of 0.005–0.06 m_H/cm^3, and M_{tot} of $1–9 \times 10^8$ $M_\odot$. While the

Table 4. Properties of the four best-fit generic models for the Local Group dSphs, Fornax, Sculptor, Sextans, and Carina.

dSphs	#	$M_{\rm tot}$	$\rho_{\rm c,gas}$	$r_{\rm max}$	$c_\star$	$\epsilon_{\rm SN}$	$t_{\rm trunc}$	L_V	⟨[Fe/H]⟩	$r_{\rm t}$	$\sigma_\star$	$\sigma_{\rm DM}$	$M_{\rm gas}$	$M_{\rm stars}$	$M_{\rm halo}$
	$10^8\,M_\odot$	$\rm m_H/cm^3$	kpc	-	-	Gyr	$10^6\,L_\odot$		kpc	$\rm km\,s^{-1}$	$\rm km\,s^{-1}$	$10^7\,M_\odot$	$10^7\,M_\odot$	$10^7\,M_\odot$	
Fornax	1335	7	0.059	7.1	0.05	0.03	–	13.9	−1.01	1.98	9.4	15.0	2.4	1.35	8.80
Sculptor	1324	5	0.029	9.6	0.05	0.03	9.1	1.50	−1.75	2.93	6.4	11.7	1.9	0.34	4.45
Sextans	1316	3	0.022	8.0	0.05	0.03	4.7	0.37	−2.09	1.58	4.2	9.7	0.5	0.07	1.04
Carina	1281	1	0.022	3.5	0.1	0.03	–	0.24	−1.93	0.76	3.1	7.2	0.2	0.02	0.63

Notes. Leftward of the vertical line are the physical input parameters of the models. Rightward of the same line are the final outputs of the models. They are calculated within the radius containing 90% of the galaxy total light.

reproduction of these global relations is a necessary step, it is however insufficient to ensure that the star formation history of the galaxies are correct.

Among these simulations, we selected a set of four models that most closely reproduce the observations. We limited as much as possible any variations in $\epsilon_{\rm SN}$ and $c_\star$. Our selection was based on comparison with the observed galaxy metallicity distribution, the V-band luminosities, the abundance ratios, and the stellar age distributions. The observed luminosities were taken from Walker et al. (2009b). The metallicity distributions were retrieved from Battaglia et al. (2011) for Sextans, from Battaglia et al. (2006), Tolstoy et al. (2004), and Helmi et al. (2006), for Fornax, Sculptor, Carina, respectively, based on the new CaT calibration of Starkenburg et al. (2010). The abundance ratios were taken from Tolstoy et al. (2009), Letarte et al. (2010), Shetrone et al. (2003), and Koch et al. (2008). The stellar age distributions were taken from Smecker-Hane et al. (1996); Hurley-Keller et al. (1998) (Carina), Babusiaux et al. (2005); Shetrone et al. (2003); Tolstoy et al. (2003) (Sculptor), Coleman & de Jong (2008) (Fornax), and Lee et al. (2003) (Sextans). A summary of the mean observed properties of the four local group dSphs is given in Table 5. It also includes the dSph tidal radii from Irwin & Hatzidimitriou (1995) as well as the velocity dispersions from Walker et al. (2009a).

Figure 13 displays our final selection. These models are shown with green squares in Fig. 12; they fall close to the observed M/L, [Fe/H], and L_V, to within a factor of two for each quantity. Table 5 provides the model parameters and outputs, and $r_{\rm t}$ is the radius encompassing 90% of the V-band luminosity. In addition, $M_{\rm gas}$, $M_{\rm star}$, $M_{\rm halo}$, and M/L are computed inside $r_{\rm t}$, while [Fe/H] is calculated as the mode of the galaxy metallicity. The stellar and dark matter velocity dispersions, $\sigma_\star$ and $\sigma_{\rm DM}$, are measured along the *line of sight*, within the effective radii (half light radius). We were careful to distinguish the dark matter and the stellar velocity dispersions, because the former is a more accurate indicator of the total mass of the system, while the observations are gathered to measure the latter.

7.1. Distinct fates for the SNeII and SNeIa feedbacks

In all systems, the star formation history depends on the balance between cooling and heating. Both SNeII and SNeIa play important roles, despite their different numbers and consequently different integrated energy feedback there being a factor of ten difference between the two.

Looking closely at the course of the galaxy evolution, one sees that star formation is ignited in the galaxy central parts. Massive stars explode rapidly as SNeII and their injections of energy counteract the increase in the central gas density, leading to a flat gas profile within ∼1 kpc. The strong and rapid energy injection of SNeII explains why the sharp initial rise in intensity of the star formation rates (see first panels in Fig. 13) is soon followed by a sharp decrease: the feedback energy acts to inhibit star formation.

Table 5. Some of the observed properties of the Local Group dSphs Fornax, Sculptor, Sextans, and Carina, which are used in the present study.

dSph	L_V	⟨[Fe/H]⟩	M/L	$r_{\rm t}$	σ
	$[10^6\,L_\odot]$			[kpc]	$[\rm km\,s^{-1}]$
Fornax	14	−1.17	12	2.08	11.7
Sculptor	1.4	−1.96	158	1.33	9.2
Sextans	0.41	−2.26	19	3.10	7.9
Carina	0.24	−1.86	88	0.58	6.6

Notes. The luminosity comes from Walker et al. (2009b). The mean metallicities were calculated from Battaglia et al. (2011) for Sextans, from Battaglia et al. (2006), Tolstoy et al. (2004), and Helmi et al. (2006), for Fornax, Sculptor, and Carina, respectively, with the new CaT calibration of Starkenburg et al. (2010). The M/L ratios were computed using the masses derived by Walker et al. (2007); Battaglia et al. (2008); Kleyna et al. (2004). The tidal and core radii are taken from Irwin & Hatzidimitriou (1995) and the velocity dispersions from Walker et al. (2009a).

Meanwhile, lower mass stars are progressively redistributed along a steep profile. Indeed, their velocity dispersion at birth is small, on the order of $5\,\rm km\,s^{-1}$, as inherited from the turbulent gas motion. Therefore, their ensemble contracts because, being decoupled from the gas, it is no longer supported by pressure. The number of SNeIa increases with time until they become the dominant source of heating in the central regions (0.2 pc) preventing gas cooling and condensing again, despite the very short cooling time. The predominance of the heating by SNeIa over that of SNeII is only possible because the former are more concentrated in space than the latter. This causes the few Gyr-long periods of very low level (or absence) of star formation after the initial 2−4 Gyr. Once the bulk of SNeIa explosions have passed, star formation is again possible at higher rates.

These phenomena have been explicitly witnessed in a Sculptor-like simulation in which the energy released by SNeIa was artificially set to zero. Star formation was then maintained to a substantial level of $0.005\,M_\odot/\rm yr$, corresponding to half of the amplitude of the first burst, where star formation had been quenched in the generic model.

7.2. Generic models

Overall, our model mean properties are in excellent agreement with the observations. This suggests that a sequence of dSphs can be reproduced by varying very few parameters. Carina, Sextans, Sculptor, and Fornax form an increasing sequence of total masses and initial central densities. All systems experience an initial ∼2 Gyr burst. Depending on the mass, the star formation

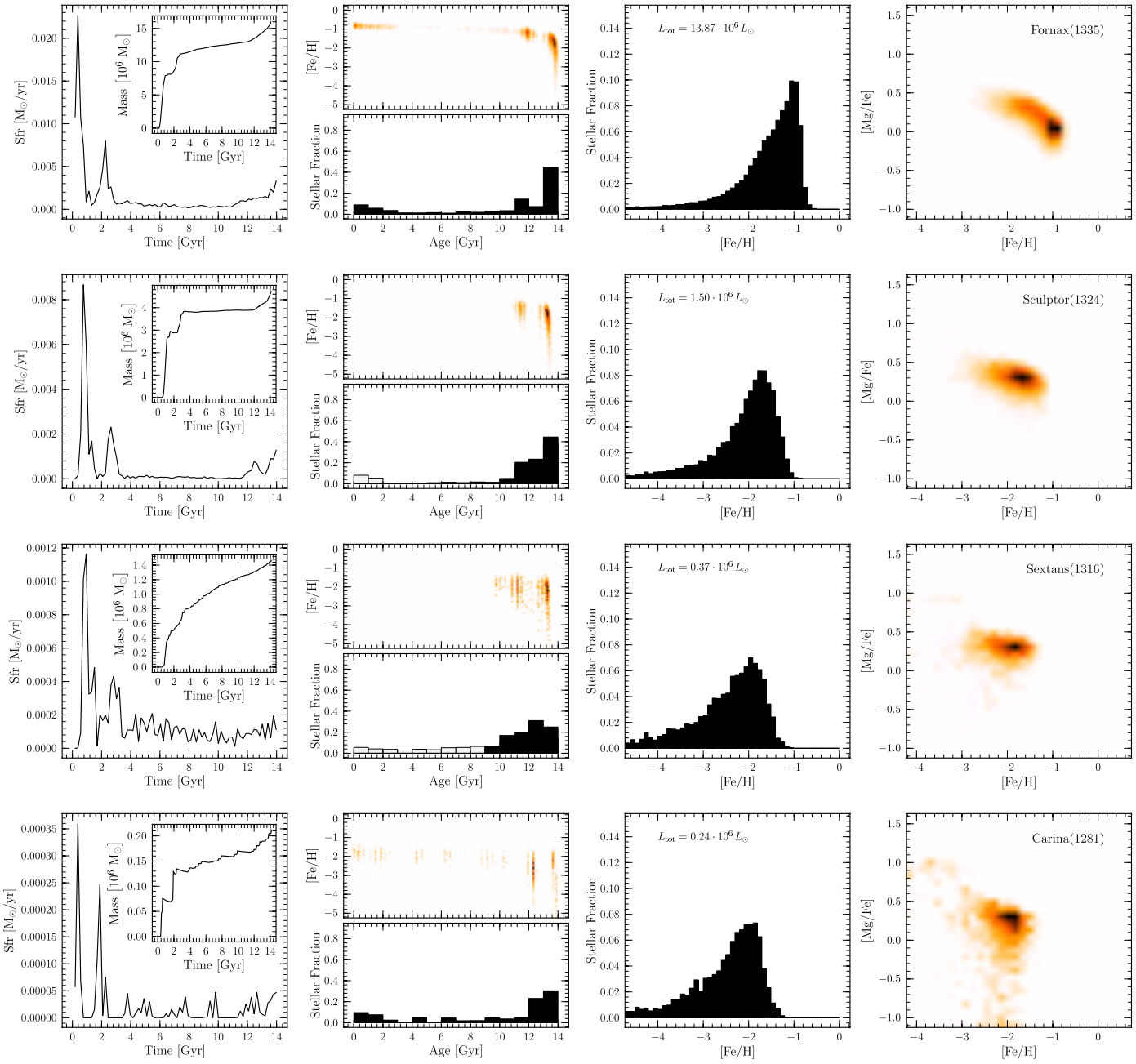

Fig. 13. Properties of the four selected models representing Fornax, Sculptor, Sextans and Carina. From left to right, the plots display, the star formation rate and the evolution of the stellar mass, the normalized stellar age distribution, together with the evolution of [Fe/H]. The final [Fe/H] distribution and ratio [Mg/Fe] as a function of [Fe/H]. The gray region in the stellar age distribution of Sculptor and Sextans correspond to the stellar population which would have been created if we would not have truncated the star formation. These populations are absent from the metallicity distributions and abundance ratios. The stellar V-band luminosities computed are 14 Gyr.

history can then be considerably reduced, or even quenched, in the case of small systems. The parameter ϵ_{SN} is fixed to 0.03, and $c_\star$ to 0.05 except for Carina. As discussed in Sect. 5.3, increasing $c_\star$ clearly leads to discontinuous star formation histories. This small difference may be the sign of some external factor in the formation of the galaxy, which was not taken into account in our models. The sequence in mass and central gas density can be understood in terms of the following considerations, at fixed $c_\star$ (∼0.05) and ϵ_{SN} (∼0.03):

- at high mass, i.e., above $\sim 3 \times 10^8\, M_\odot$. The evolution of the systems is quite uniform. The cooling always dominates the feedback and the virial temperature reaches 10^4 K around which the radiative cooling is very strong. Hence, the star formation is never completely quenched;
- the diversity of evolutionary paths is larger for lower mass systems. Those who initially form a large quantity of stars in proportion to their total mass, do release high SNeIa-driven feedback energy, which is able to counterbalance their cooling. The level at which star formation is quenched depends on the ratio of the cooling to the energy released by SNeIa, following the process described in Sect. 7.1. This ratio reflects the level at which the galaxy has used its full capacity to form stars during the first Gyr, i.e., the fraction of gas transformed into stars, as determined by the galaxy mass and

initial central density. Low mass and low central gas density systems have a rather long cooling time (>1 Gyr). The SNeII are sufficient to completely quench momentarily the star formation, which needs more than 1 Gyr to be reignited, and proceeds episodically.

The four models reproducing the observed properties of Carina, Sextans, Sculptor, and Fornax follow these rules. An additional feature is that the choice ϵ_{SN} (primarily) and $c_\star$ was definitely driven by Fornax. Its luminosity and mass require a vigorous and continuous star formation, in turn forcing both parameters to be low.

As in Revaz et al. (2009), our models retain a large fraction of their gas, from 10^6 to $10^7\,M_\odot$ and in inverse proportion to the galaxy stellar mass, i.e., low stellar mass systems have the largest fraction of gas at 14 Gyr. Moreover, both Sextans and Sculptor models need to have their star formation artificially stopped, respectively, at ~5 and ~9 Gyr. The low ϵ_{SN} and $c_\star$ imposed by Fornax are inefficient in quenching it either by means of thermal SNe feedback or even galactic winds. This strongly supports stripping of the gas by external gravitational and/or hydrodynamical interactions (see for example, Mayer et al. 2006), even though the bulk of the galaxy formation could be determined by their initial conditions.

8. Spatial distribution of the stellar populations

The presence of metallicity gradients in dSphs is debated. Evidence of stellar population segregation has been reported in Sculptor (Tolstoy et al. 2004), Fornax (Battaglia et al. 2006), and Sextans (Battaglia et al. 2011). In these galaxies, the most metal-rich stars are concentrated at the galaxy central regions, while the metal-poor ones are essentially found at every radius. In contrast, no radial change in the metallicity is found in LeoI (Koch et al. 2007b; Bosler et al. 2007; Gullieuszik et al. 2009), LeoII (Koch et al. 2007a), and CVnI (Ural et al. 2010). Kirby et al. (2011) reported shallow metallicity gradients of at most −0.21 dex per core radius in LeoII .

Figure 14 presents the radial [Fe/H] density maps for our four generic models. They show no evidence of any radial change in metallicity distribution. This is a common feature to all our models. In the following, we examine the gas motion leading to the final structure of our model galaxies and consider two of our very high resolution simulations containing 4′194′304 particles with an initial total mass of $3 \times 10^8\,M_\odot$ and $9.5 \times 10^8\,M_\odot$, from Table 1.

The $3 \times 10^8\,M_\odot$ model is characterized by two strong episodes of star formation (see the top of Fig. 4). The first one occurs between 0.4 and 1.6 Gyr, the second one, slightly weaker, takes place between 2.1 Gyr and 3.2 Gyr. The physical processes described in the following apply to any other model with a low mass. Figure 15 displays the radial [Fe/H] density maps of the gas during the first period of star formation. The metallicity gradient seen in the first snapshot at $t = 0.8$ Gyr is the consequence of the first generations of stars forming preferentially in the galaxy central high density regions, hence leading to greater chemical enrichment. This implies that for a short period of time, stellar evolution occurs on shorter timescales than the gas motion. The gradient persists at $t = 1.4$ Gyr, although being already shallower, but soon after it disappears.

Figure 16 presents the physical mechanisms at play. As seen in the upper panel, the gas accumulates in the central regions during a period of intense star formation, not only metals but also the thermal energy released by the explosions SNeII.

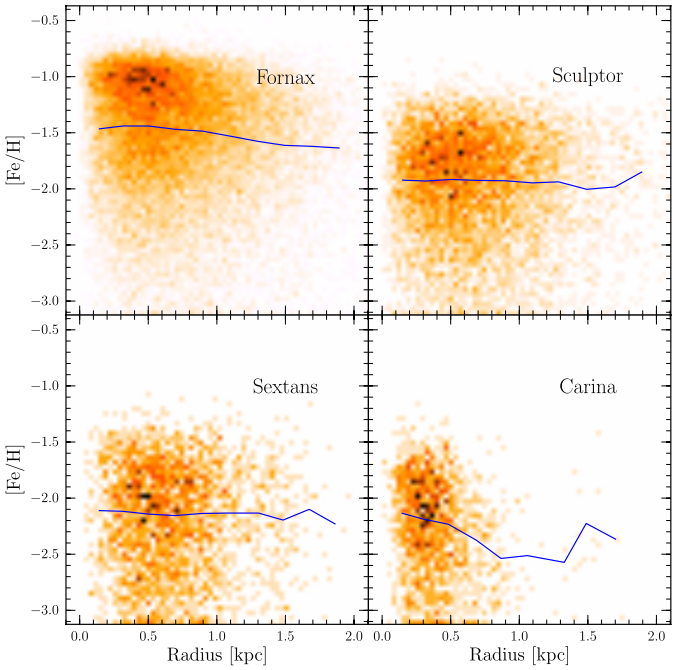

Fig. 14. The radial distribution of the stellar [Fe/H] for our four selected generic models. Each panel is a 2D histogram of the number of particles weighted by their mass. The blue curve follows the mean value of [Fe/H] computed at each radius bin.

Consequently, the gas is hotter and more tenuous than its surroundings (see snapshot at $t = 1.4$ Gyr) and forms a bubble. Very strong Archimedes forces act in the vicinity of the center of the galaxy potential well, making the position of the bubble unstable. Small motions induced by the local turbulence are sufficient to offset the bubble and cause it to be quickly dragged outward. This phenomenon is seen twice: first between 1.5 and 1.7 Gyr, then between 1.7 and 2 Gyr. The hot and metal-rich gas bubble (seen in red in Fig. 16) leaves the main body of the galaxy, reaching regions out to 10 kpc. Subsequent episodes of star formation would experience the same scenario, erasing any metallicity gradient in the gas in less than a Gyr. We note that the uplift of hot bubbles by Archimedes forces is a common mechanism in cooling flow clusters (Revaz et al. 2008).

The evolution of the $9.5 \times 10^8\,M_\odot$ model is displayed at the bottom of Fig. 16. A gradient in metallicity is visible between 1.1 and 1.7 Gyr. The fundamental difference from the former example is that here stars efficiently form in a much wider region. Metals and feedback energy are then injected across a larger volume. Therefore, turbulent motions are sufficiently strong to erase the initial gradients.

In summary, our high resolution simulations show that the hot gas motions have very short timescales of evolution that are incompatible with the formation of a stellar metallicity gradient. We note that our simulations do not include mixing in the interstellar medium. This would increase the dilution of any differential spatial metallicity distribution. In contrast, a multi-phase and multi-scale structure of the interstellar medium may prevent the formation and migration of hot bubbles. This probably deserves future investigation. As discussed in Sect. 5.1, the effect of our feedback is rather small. In principle, a stronger feedback would increase the turbulence of the ISM and also act to remove metallicity gradients.

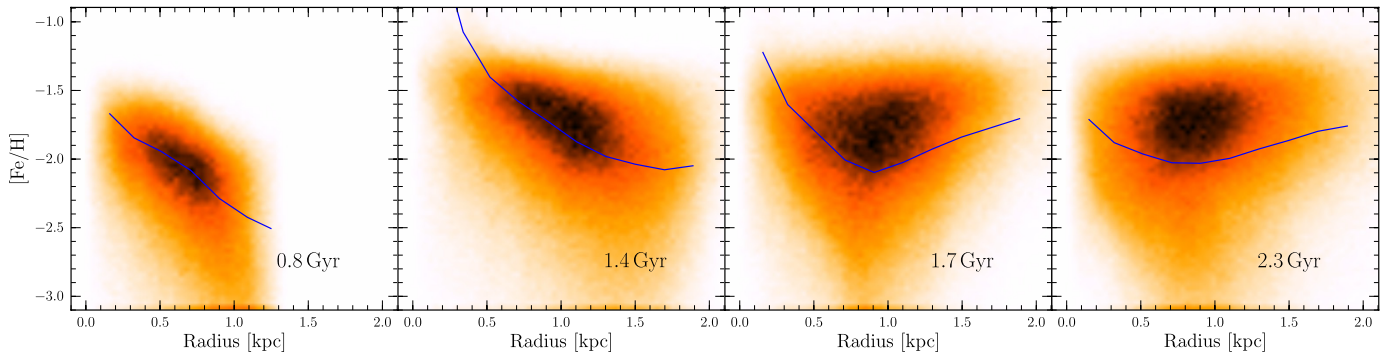

Fig. 15. Evolution of the stellar metallicity gradient with time for a 3×10^8 $M_\odot$ model containing 4′194′304 particles. As in Fig. 14, each plot corresponds to a 2D histogram of the number of particles weighted by their mass.

9. The stellar mass fractions in *N*-body simulation dark matter halos

The final baryonic fraction $f_{\rm bf}$ is an interesting quantity, since it can be observationally derived in galaxies and is different from the initial cosmological one. Within the radius containing 90% of the stars, this fraction varies in our models from 25% to 35%. Considering the stellar baryonic mass, it ranges from 2% to 10%, as for the results of Valcke et al. (2008), who also developed models of galaxies in isolation.

Looking at $M_{\rm stars}/M_{\rm halo}$, Sawala et al. (2011) compared the predictions of a series of *N*-body models of galaxies with the expected ratios calculated from the Sloan Digital Sky Survey (SDSS) for the stellar part and from the MilleniumII simulation for the pure dark matter content (Guo et al. 2011). The dependence of $M_{\rm stars}/M_{\rm halo}$ on $M_{\rm halo}$ was originally performed for stellar masses between $10^{8.3}$ $M_\odot$ and $10^{11.8}$ $M_\odot$. It was then extrapolated from $10^{8.3}$ $M_\odot$ down to 10^6 $M_\odot$. Doing so, Sawala et al. (2011) found the fraction of stellar baryons in dark halo masses below 10^{10} $M_\odot$ to be lower in the SDSS/MilleniumII predictions than in the galaxy models. Their interpretation was that galaxy models may produce too many stars. This conclusion deserves further consideration.

Figure 17 present the predictions of Sawala et al. (2011) as observable quantities. The relation of Guo et al. (2011) between galaxy stellar and halo masses has been converted here into *V*-band luminosities and velocity dispersions. Following Sawala et al. (2011), we considered two different slopes for the faint-end of the stellar mass function, −1.15 (Li & White 2009) and −1.58 (Baldry et al. 2008). We converted stellar masses into luminosities by assuming a reasonable stellar $M_{\rm stars}/L_V$ ratio of 0.75 (Flynn et al. 2006). As the observed V-band luminosities vary over several dex, the uncertainties in $M_{\rm stars}/L_V$ hardly affect our results. The correspondence between the halo masses and their velocities was computed in two ways. First, we used the relation between the maximal velocity and halo mass measured in the Aquarius project (Springel et al. 2008). Second, we assumed an NFW profile and solved numerically the Jeans equations in spherical coordinates following Eq. (11), and considering extreme values, 5 and 30, for the profile concentration (Macciò et al. 2007). The velocity dispersions extracted from the inner 1 kpc are computed by properly taking into account projection effects.

The comparison between the observations of dwarf galaxies (Mateo 1998), as well as irregular, elliptical, and spiral galaxies from Garrido et al. (2002) and the SAURON sample (de Zeeuw et al. 2002), and a range of different *N*-body simulations (Sawala et al. 2011; Stinson et al. 2007, 2009; Valcke et al. 2008; Governato et al. 2010; Pelupessy et al. 2004) permits us to make the following remarques. Noteworthily, the agreement between all models of small mass systems on the one hand and their consistency with the observations on the other hand is quite remarkable, despite the considerable variations in the assumption, including the initial conditions, from cosmological to isolation. Where stellar masses were actually measured in the SDSS, the consistency of the relation of Guo et al. (2011) with the observations is very good indeed. In contrast, at lower masses, the discrepancy with Sawala et al. (2011)'s extrapolation is very large. Whilst the observed velocities are derived from baryonic matter and might be lower than the dark matter halo ones by a factor of two (see Table 4), this is insufficient to fill in the gap between the SDSS/MilleniumII relation and the observations. Similarly, varying the stellar $M_{\rm stars}/L_V$ even by a factor of ten does not help either.

The velocity dispersion of the stellar component also depends on its density profile, which could well be different from the dark matter one. Therefore, we performed some tests assuming different profiles for the stars and the dark halos. For the stellar density profile, we took a truncated plummer sphere (e.g., Battaglia et al. 2006, 2008), while the dark matter density profile was kept to the NFW form. We calculated the inner 1kpc velocity dispersions of both components, which agree to within a few percent. This is much smaller than the mean factors observed in Fig. 17.

In summary, the relation between $M_{\rm stars}$ derived from observed luminosities, color, spectroscopy etc., and $M_{\rm halo}$ from pure dark matter simulations should be revisited. The assumptions under which the number density of galaxies and dark matter halos match each other (Guo et al. 2011) lead to inconsistency with the observations at low stellar masses.

10. Conclusions

We have described our new parallel Nbody/Tree-SPH code, `GEAR`. Starting from the public version of `Gadget-2`, we have included the physics of baryons, i.e., metal-dependent gas cooling, star formation recipes, thermal feedback driven by Type Ia and Type II supernova explosions, and chemical evolution. We designed `GEAR` to ensure a high spatial resolution together with detailed chemical diagnostics, and to follow the galaxy evolution over a full Hubble time, either in isolation or in a cosmological context. We have qualified its performances in the case of dSph galaxies.

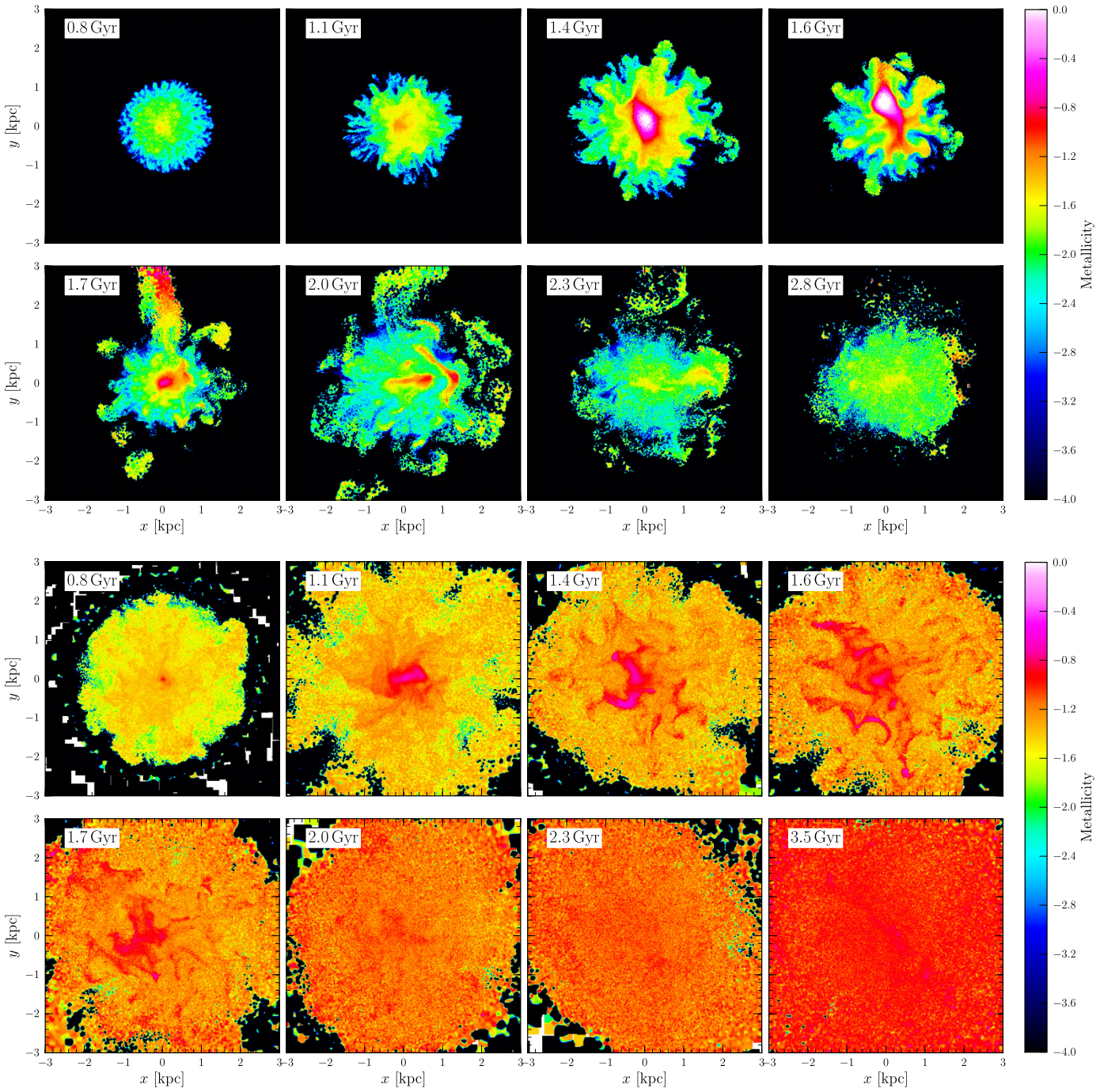

Fig. 16. Evolution of the metallicity with time. Top, model with a total mass of $3 \times 10^8\,M_\odot$. Bottom, the one with $9.5 \times 10^8\,M_\odot$. The maps corresponds to a thin slice of 0.1 kpc. The colors code [Fe/H], from −4 to 0.

▷ GEAR conserves the total energy of the systems to better than 5% over 14 Gyr. Moreover, the code provides an excellent convergence of the results with numerical resolution. We have been able to show that for small galactic systems, such as dSphs, 2^{16} particles offer a good trade-off between CPU time and resolution, catching the essence of the physics at play and allowing secure predictions.

▷ Varying the initial random number seed, we have estimated that our intrinsic errors are below 30% in the model stellar masses, the V-band luminosities, and mode metallicities.

▷ Hundreds of simulations were performed in order to understand and quantify the effect of the free parameters, such as the star formation parameter ($c_\star$), the star formation density threshold ($\rho_{\rm sfr}$), the supernova efficiency ($\epsilon_{\rm SN}$), the number of stellar particles formed from each gas particle ($N_\star$), the adiabatic period ($t_{\rm ad}$) attached to the thermal feedback,and the number of particles in a softening radius ($N_{\rm ngb}$). The most sensitive parameter is definitely $\epsilon_{\rm SN}$, with acceptable values ranging from 0.03 and 0.05 enabling us to reproduce the sequence of dSphs. These low values imply that strong winds are incompatible with their observed metallicities.

▷ We ran a 512^3 ΛCDM cosmological simulation of pure dark matter in order to study the profiles of halos with masses between 10^8 and $10^9\,M_\odot$, which are typical of dSphs. The

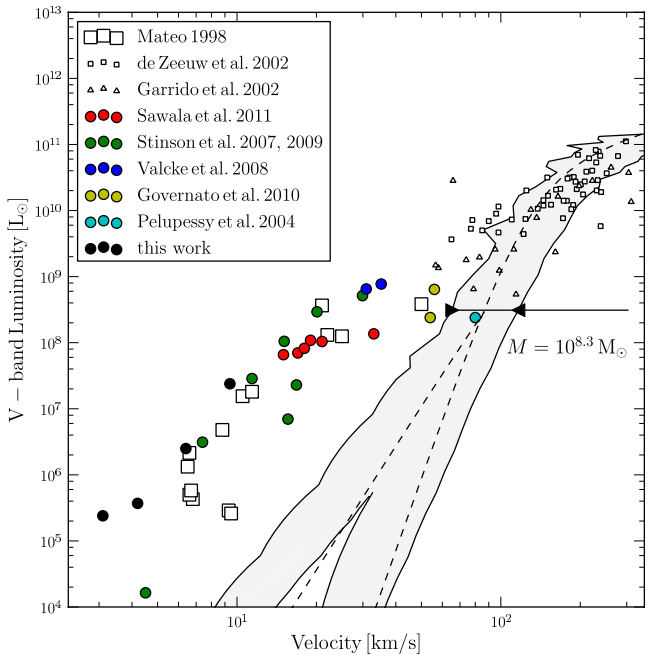

Fig. 17. The relation between the galaxy velocity dispersions or maximal velocities and their V-band luminosities. Filled circles correspond to the results of this work and those of N-body simulations. The observations of low-mass galaxies are displayed with open symbols. The gray area indicates how the Guo et al. (2011)'s relation between stellar and dark halo masses, further extrapolated by Sawala et al. (2011), translates into luminosities and velocity dispersions for a minimum and maximum value of the NFW concentration parameter. Below a stellar mass of $10^{8.3}$ $M_\odot$, two faint end slopes of stellar mass functions are considered (see text), splitting in two different branches the gray area. The dashed black lines are obtained when considering the Aquarius project's relation between the maximal velocity and halo mass (Springel et al. 2008). The minimum stellar mass ($10^{8.3}$ $M_\odot$) for the original Guo et al. (2011)'s fit and its correspondence in terms of range of velocities is indicated with black arrows.

expansion of the Universe leads to the formation of stable systems after $z = 6$. In turn, this justifies models of dSphs in a static Euclidean space, where the expansion of the universe is neglected. The physics of baryons that depends on the density in physical coordinates is correct. We showed that halos experiencing only minor mergers since $z = 6$ do exist. Whilst at fixed mass the densities of these halos are very similar, they still exhibit a small dispersion (of a factor of between three and four).

▷ We have confirmed that the total initial galaxy mass plays a critical role in the evolution of the galaxies. However, we have also demonstrated that the initial central gas density is as crucial. Changing the mass by a factor of ten leads to a change of a few tenths of a dex in the final mean metallicity, while a factor of ten in central density can increase [Fe/H] by more than 1 dex. We have shown that the Local Group classical dSph could have their properties reproduced as a sequence of mass and density.

▷ The differences that we have found in mass and initial gas central densities seen in the ΛCDM simulation lead to a variety of star formation histories explaining the diversity of the chemical properties observed in dSphs. In massive and dense systems, the cooling dominates the feedback, and stars are formed continuously, leading to luminous and metal-rich galaxies. At lower masses, the variety of star formation results from the subtle balance between the cooling and supernovae feedback of both SNeIa and SNeII. Gas is still present in our model galaxies with masses from about 10^6 to 10^7 $M_\odot$ after 14 Gyr. This strongly supports the existence of external processes such as tidal or ram pressure stripping, which we did not include in this study.

▷ Because SNeIa and SNeII have different spatial distributions, they act in distinct ways in the heating of the systems. In particular, we showed that the few Gyr-long quiescent periods of star formation are due to the explosion of the centrally concentrated SNeIa.

▷ We have investigated the relationship between the stellar mass of galaxies and their parent dark matter halos. The agreement between all models of small mass systems on the one hand and with the observations on the other hand is quite remarkable, despite the considerable variations in the assumptions, including the initial conditions, from a cosmological context to isolation. They are consistent with the observations.

▷ Despite the new stars being preferentially formed in the galaxy central regions, none of our models display any segregation in stellar population, such as the metal-rich stars being more centrally concentrated than the less metallic ones, as reported in some observations. We have shown how turbulence in massive systems and uplifted hot metal-rich bubbles in less massive ones do erase the initial metallicity gradients seen in the gas at ages younger than 2 Gyr. Further investigations are definitely required to explain the metallicity gradients reported in some of the classical dSphs.

Acknowledgements. P.J. and Y.R. were stimulated by the vivid escort of the DART collaboration. They are grateful to Volker Springel for making `Gadget-2` publicly available and for providing complete and clear documentation. This work was supported by the Swiss National Science Foundation. The authors thank the International Space Science Institute (ISSI) at Bern for their funding of the team "Defining the full life-cycle of dwarf galaxy evolution: the Local Universe as a template".

References

Alimi, J.-M., Serna, A., Pastor, C., & Bernabeu, G. 2003, J. Comput. Phys., 192, 157
Anders, E., & Grevesse, N. 1989, Geochim. Cosmochim. Acta, 53, 197
Babusiaux, C., Gilmore, G., & Irwin, M. 2005, MNRAS, 359, 985
Baldry, I. K., Glazebrook, K., & Driver, S. P. 2008, MNRAS, 388, 945
Battaglia, G., Tolstoy, E., Helmi, A., Tolstoy, E., et al. 2006, A&A, 459, 423
Battaglia, G., Helmi, A., Tolstoy, E., et al. 2008, ApJ, 681, L13
Battaglia, G., Tolstoy, E., Helmi, A., et al. 2011, MNRAS, 411, 1013
Beuther, H., Churchwell, E. B., McKee, C. F., & Tan, J. C. 2007, Protostars and Planets V, 165
Binney, J., & Tremaine, S. 1987, Galactic dynamics (Princeton, NJ: Princeton University Press), 747
Blais-Ouellette, S., Amram, P., & Carignan, C. 2001, AJ, 121, 1952
Bosler, T. L., Smecker-Hane, T. A., & Stetson, P. B. 2007, MNRAS, 378, 318
Brook, C. B., Kawata, D., Gibson, B. K., & Flynn, C. 2004, MNRAS, 349, 52
Carraro, G., Chiosi, C., Girardi, L., & Lia, C. 2001, MNRAS, 327, 69
Coleman, M. G., & de Jong, J. T. A. 2008, ApJ, 685, 933
Dalla Vecchia, C., & Schaye, J. 2008, MNRAS, 387, 1431
de Blok, W. J. G. 2005, ApJ, 634, 227
de Blok, W. J. G., & Bosma, A. 2002, A&A, 385, 816
de Blok, W. J. G., Walter, F., Brinks, E., et al. 2008, AJ, 136, 2648
de Zeeuw, P. T., Bureau, M., Emsellem, E., et al. 2002, MNRAS, 329, 513
Eisenstein, D. J., & Hut, P. 1998, ApJ, 498, 137
Flynn, C., Holmberg, J., Portinari, L., Fuchs, B., & Jahreiß, H. 2006, MNRAS, 372, 1149
Garrido, O., Marcelin, M., Amram, P., & Boulesteix, J. 2002, A&A, 387, 821
Gentile, G., Salucci, P., Klein, U., Vergani, D., & Kalberla, P. 2004, MNRAS, 351, 903
Gentile, G., Burkert, A., Salucci, P., Klein, U., & Walter, F. 2005, ApJ, 634, L145
Gerritsen, J. P. E. 1997, Ph.D. Thesis, Groningen University, The Netherlands
Governato, F., Brook, C., Mayer, L., et al. 2010, Nature, 463, 203
Gullieuszik, M., Held, E. V., Saviane, I., & Rizzi, L. 2009, A&A, 500, 735
Guo, Q., White, S., Boylan-Kolchin, M., et al. 2011, MNRAS, 413, 101
Helmi, A., Irwin, M. J., Tolstoy, E., et al. 2006, ApJ, 651, L121
Hernquist, L. 1993, ApJS, 86, 389
Hinshaw, G., Weiland, J. L., Hill, R. S., et al. 2009, ApJS, 180, 225
Hultman, J., & Pharasyn, A. 1999, A&A, 347, 769

Hurley-Keller, D., Mateo, M., & Nemec, J. 1998, AJ, 115, 1840
Irwin, M., & Hatzidimitriou, D. 1995, MNRAS, 277, 1354
Iwamoto, K., Brachwitz, F., Nomoto, K., et al. 1999, ApJS, 125, 439
Katz, N. 1992, ApJ, 391, 502
Katz, N., Weinberg, D. H., & Hernquist, L. 1996, ApJS, 105, 19
Kawata, D., & Gibson, B. K. 2003, MNRAS, 340, 908
Kawata, D., Arimoto, N., Cen, R., & Gibson, B. K. 2006, ApJ, 641, 785
Kennicutt, Jr., R. C. 1998, ApJ, 498, 541
Kirby, E. N., Lanfranchi, G. A., Simon, J. D., Cohen, J. G., & Guhathakurta, P. 2011, ApJ, 727, 78
Kleyna, J. T., Wilkinson, M. I., Evans, N. W., & Gilmore, G. 2004, MNRAS, 354, L66
Kobayashi, C., Tsujimoto, T., & Nomoto, K. 2000, ApJ, 539, 26
Koch, A., Grebel, E. K., Kleyna, J. T., et al. 2007a, AJ, 133, 270
Koch, A., Wilkinson, M. I., Kleyna, J. T., et al. 2007b, ApJ, 657, 241
Koch, A., Grebel, E. K., Gilmore, G. F., et al. 2008, AJ, 135, 1580
Kodama, T., & Arimoto, N. 1997, A&A, 320, 41
Komatsu, E., Dunkley, J., Nolta, M. R., et al. 2009, ApJS, 180, 330
Kroupa, P. 2001, MNRAS, 322, 231
Lee, M. G., Park, H. S., Park, J.-H., et al. 2003, AJ, 126, 2840
Leitherer, C., Robert, C., & Drissen, L. 1992, ApJ, 401, 596
Letarte, B., Hill, V., Tolstoy, E., et al. 2010, A&A, 523, A17
Li, C., & White, S. D. M. 2009, MNRAS, 398, 2177
Macciò, A. V., Dutton, A. A., van den Bosch, F. C., et al. 2007, MNRAS, 378, 55
Maio, U., Dolag, K., Ciardi, B., & Tornatore, L. 2007, MNRAS, 379, 963
Marcolini, A., D'Ercole, A., Brighenti, F., & Recchi, S. 2006, MNRAS, 371, 643
Marcolini, A., D'Ercole, A., Battaglia, G., & Gibson, B. K. 2008, MNRAS, 386, 2173
Marri, S., & White, S. D. M. 2003, MNRAS, 345, 561
Mateo, M. L. 1998, ARA&A, 36, 435
Mayer, L., Mastropietro, C., Wadsley, J., Stadel, J., & Moore, B. 2006, MNRAS, 369, 1021
Merlin, E., Buonomo, U., Grassi, T., Piovan, L., & Chiosi, C. 2010, A&A, 513, A36
Mori, M., Yoshii, Y., Tsujimoto, T., & Nomoto, K. 1997, ApJ, 478, L21
Navarro, J. F., & White, S. D. M. 1993, MNRAS, 265, 271
Navarro, J. F., Frenk, C. S., & White, S. D. M. 1996, ApJ, 462, 563
Navarro, J. F., Frenk, C. S., & White, S. D. M. 1997, ApJ, 490, 493
Oh, S.-H., de Blok, W. J. G., Brinks, E., Walter, F., & Kennicutt, Jr., R. C. 2011, AJ, 141, 193
Okamoto, T., Frenk, C. S., Jenkins, A., & Theuns, T. 2010, MNRAS, 406, 208
Omont, A. 2007, Reports on Progress in Physics, 70, 1099
Pelupessy, F. I., van der Werf, P. P., & Icke, V. 2004, A&A, 422, 55
Read, J. I., Pontzen, A. P., & Viel, M. 2006, MNRAS, 371, 885
Revaz, Y., Combes, F., & Salomé, P. 2008, A&A, 477, L33
Revaz, Y., Jablonka, P., Sawala, T., et al. 2009, A&A, 501, 189
Ricotti, M., & Gnedin, N. Y. 2005, ApJ, 629, 259
Saitoh, T. R., & Makino, J. 2009, ApJ, 697, L99
Saitoh, T. R., Daisaka, H., Kokubo, E., et al. 2008, PASJ, 60, 667
Salpeter, E. E. 1955, ApJ, 121, 161
Sawala, T., Scannapieco, C., Maio, U., & White, S. 2010, MNRAS, 402, 1599
Sawala, T., Guo, Q., Scannapieco, C., Jenkins, A., & White, S. 2011, MNRAS, 413, 659
Scannapieco, C., Tissera, P. B., White, S. D. M., & Springel, V. 2005, MNRAS, 364, 552
Scannapieco, C., Tissera, P. B., White, S. D. M., & Springel, V. 2006, MNRAS, 371, 1125
Schmidt, M. 1959, ApJ, 129, 243
Schroyen, J., De Rijcke, S., Valcke, S., Cloet-Osselaer, A., & Dejonghe, H. 2011, MNRAS, 416, 601
Serna, A., Alimi, J.-M., & Chieze, J.-P. 1996, ApJ, 461, 884
Shetrone, M., Venn, K. A., Tolstoy, E., et al. 2003, AJ, 125, 684
Smecker-Hane, T. A., Stetson, P. B., Hesser, J. E., & Vandenberg, D. A. 1996, in From Stars to Galaxies: the Impact of Stellar Physics on Galaxy Evolution, ed. C. Leitherer, U. Fritze-von-Alvensleben, & J. Huchra, ASP Conf. Ser., 98, 328
Sommer-Larsen, J., Götz, M., & Portinari, L. 2003, ApJ, 596, 47
Spano, M., Marcelin, M., Amram, P., et al. 2008, MNRAS, 383, 297
Spekkens, K., Giovanelli, R., & Haynes, M. P. 2005, AJ, 129, 2119
Springel, V. 2005, MNRAS, 364, 1105
Springel, V., & Hernquist, L. 2002, MNRAS, 333, 649
Springel, V., & Hernquist, L. 2003, MNRAS, 339, 289
Springel, V., Yoshida, N., & White, S. D. M. 2001, New Astron., 6, 79
Springel, V., Wang, J., Vogelsberger, M., et al. 2008, MNRAS, 391, 1685
Starkenburg, E., Hill, V., Tolstoy, E., et al. 2010, A&A, 513, A34
Stinson, G., Seth, A., Katz, N., et al. 2006, MNRAS, 373, 1074
Stinson, G. S., Dalcanton, J. J., Quinn, T., Kaufmann, T., & Wadsley, J. 2007, ApJ, 667, 170
Stinson, G. S., Dalcanton, J. J., Quinn, T., et al. 2009, MNRAS, 395, 1455
Summers, F. 1984, Ph.D. Thesis, Univ. California, Berkeley
Sutherland, R. S., & Dopita, M. A. 1993, ApJS, 88, 253
Swaters, R. A., Madore, B. F., van den Bosch, F. C., & Balcells, M. 2003, ApJ, 583, 732
Tasker, E. J., & Bryan, G. L. 2006, ApJ, 641, 878
Tasker, E. J., & Bryan, G. L. 2008, ApJ, 673, 810
Thacker, R. J., & Couchman, H. M. P. 2000, ApJ, 545, 728
Tolstoy, E., Venn, K. A., Shetrone, M., et al. 2003, AJ, 125, 707
Tolstoy, E., Irwin, M. J., Helmi, A., et al. 2004, ApJ, 617, L119
Tolstoy, E., Hill, V., & Tosi, M. 2009, ARA&A, 47, 371
Tornatore, L., Borgani, S., Dolag, K., & Matteucci, F. 2007, MNRAS, 382, 1050
Tsujimoto, T., Nomoto, K., Yoshii, Y., et al. 1995, MNRAS, 277, 945
Ural, U., Wilkinson, M. I., Koch, A., et al. 2010, MNRAS, 402, 1357
Valcke, S., de Rijcke, S., & Dejonghe, H. 2008, MNRAS, 389, 1111
Vazdekis, A., Casuso, E., Peletier, R. F., & Beckman, J. E. 1996, ApJS, 106, 307
Walker, M. G., & Peñarrubia, J. 2011, ApJ, 742, 20
Walker, M. G., Mateo, M., Olszewski, E. W., et al. 2007, ApJ, 667, L53
Walker, M. G., Mateo, M., & Olszewski, E. W. 2009a, AJ, 137, 3100
Walker, M. G., Mateo, M., Olszewski, E. W., et al. 2009b, ApJ, 704, 1274
Wiersma, R. P. C., Schaye, J., Theuns, T., Dalla Vecchia, C., & Tornatore, L. 2009, MNRAS, 399, 574
Yepes, G., Kates, R., Khokhlov, A., & Klypin, A. 1997, MNRAS, 284, 235

Pages 19 to 28 are available in the electronic edition of the journal at http://www.aanda.org

Appendix A: Metal ejection and energy conservation

In this appendix, we describe precisely how the velocities of the neighboring stellar particles i are modified in order to improve the conservation of energy.

The mass received by the particle j is

$$m'_j = m_j + w_{ij}\, M_{\rm e}, \tag{A.1}$$

where $M_{\rm e}$ is the mass ejected by the stellar particle i. Similarly, the mass of element k is

$$m'_j(k) = m_j(k) + w_{ij}\, M_{\rm e}(k), \tag{A.2}$$

where w_{ij} is

$$w_{ij} = \frac{m_j W(r_{ij}, h_i)}{\rho_i}. \tag{A.3}$$

The final mass the the stellar particle i is

$$m'_i = m_i - M_{\rm e}. \tag{A.4}$$

As the mass of particles changes, to conserve the total energy, it is necessary to modify the velocities of the particles. We neglect to correct the change in potential energy. Before the mass redistribution, the energy of the particles involved is

$$E = \sum_j \frac{1}{2} m_j v_j^2 + \frac{1}{2} m_i v_i^2, \tag{A.5}$$

and after, it is

$$E' = \sum_j \frac{1}{2} m_j v_j'^2 + \sum_j \frac{1}{2} w_{ij}\, M_{\rm e} v_j'^2 + \frac{1}{2} m_i v_i^2 - \frac{1}{2} M_{\rm e} v_i^2, \tag{A.6}$$

where we have assumed that the particle i does not change its velocity. If $v_j'^2$ are chosen such that

$$\frac{1}{2} m_j v_j'^2 + \frac{1}{2} w_{ij}\, M_{\rm e} v_j'^2 = \frac{1}{2} m_j v_j^2 + \frac{1}{2} w_{ij}\, M_{\rm e} v_i^2, \tag{A.7}$$

the summing over j gives

$$\sum_j \frac{1}{2} m_j v_j'^2 + \sum_j \frac{1}{2} w_{ij}\, M_{\rm e} v_j'^2 = \sum_j \frac{1}{2} m_j v_j^2 + \frac{1}{2} M_{\rm e} v_i^2, \tag{A.8}$$

which implies that

$$E' = E. \tag{A.9}$$

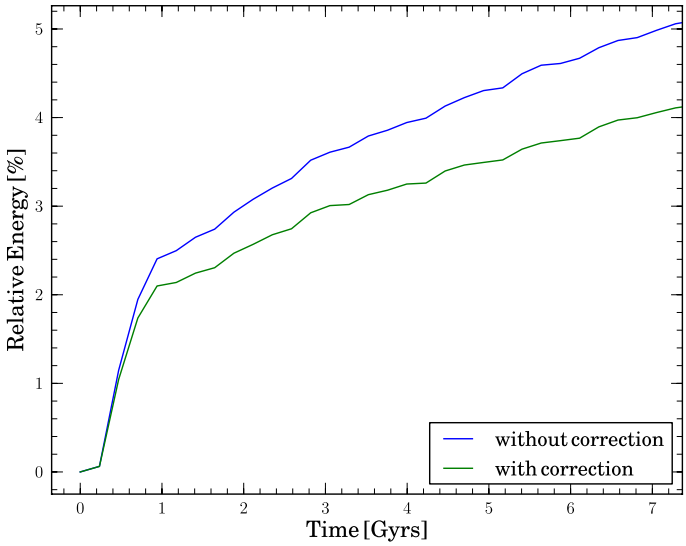

Fig. A.1. Evolution of the relative energy as a function of time. The green curve corresponds to the model presented in Fig. 3. It includes the velocity correction while the blue one is similar but uncorrected.

The new velocity for each particle is deduced from Eq. (A.7)

$$v_j'^2 = \frac{m_j v_j^2 + w_{ij}\, M_{\rm e} v_i^2}{m_j + w_{ij}\, M_{\rm e}} = \frac{m_j}{m'_j} v_j^2 + \frac{w_{ij}\, M_{\rm e}}{m'_j} v_i^2. \tag{A.10}$$

The modification of the square of the velocity is caused by chages in two terms. The velocity is first decreased, owing to the increase in the mass of the particle. The second term corresponds to the decrease in energy of particle i caused by its decrease in mass. As in practice $w_{ij}\, M_{\rm e}$ is much smaller that m_j, the change in velocity is small. Only the norm of the velocity is affected during the modification of the velocities.

The effect of this correction on the total energy is estimated by running the same simulation used in Fig. 3, but with the correction switched off. The comparison of the evolution of the relative energy is given in Fig. A.1. The improvement is about 20% over 7 Gyr, while its increase in CPU time is insignificant.

We did not observe any improvement in the linear momentum conservation. This is related to the poor conservation of the `treecode` method that does not fulfill Newton's third law and dominates the error.

Appendix B: Free parameters

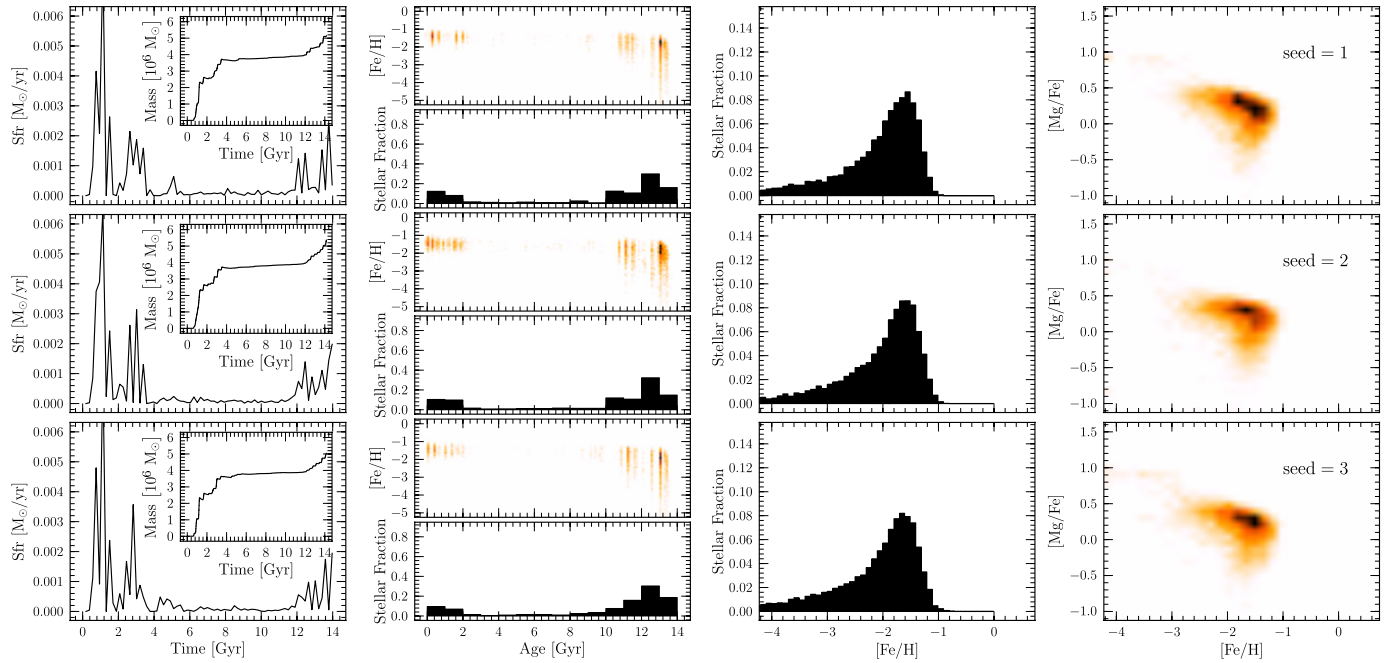

Fig. B.1. Effect of the random number seed. The parameters for the initial conditions are $M_{\rm tot} = 8 \times 10^8\,M_\odot$, $\rho_{\rm c,gas} = 0.029\,{\rm m_H/cm^3}$, and $r_{\rm max} = 8\,{\rm kpc}$. The parameters for the star formation and supernova feedback are $c_\star = 0.1$ and $\epsilon_{\rm SN} = 0.05$.

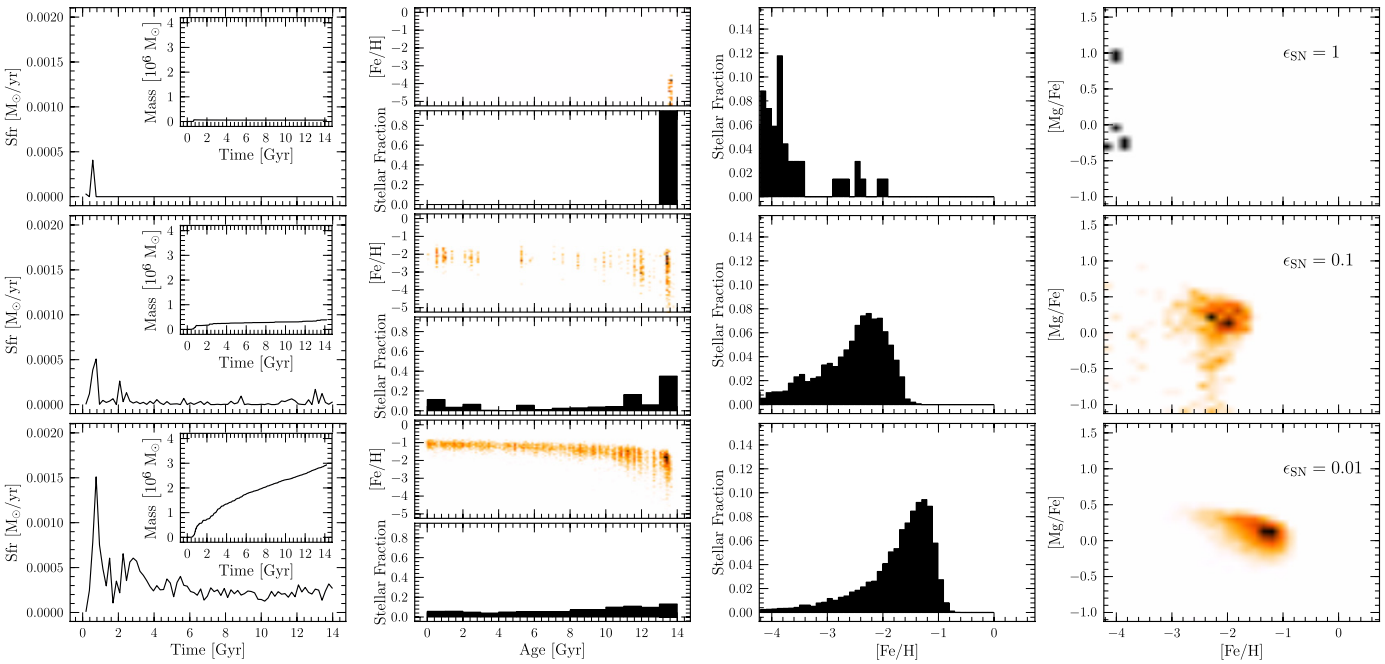

Fig. B.2. Effect of supernova efficiency $\epsilon_{\rm SN}$. The parameters for the initial conditions are $M_{\rm tot} = 3 \times 10^8\,M_\odot$, $\rho_{\rm c,gas} = 0.022\,{\rm m_H/cm^3}$, and $r_{\rm max} = 8\,{\rm kpc}$. The parameter for the star formation is $c_\star = 0.03$.

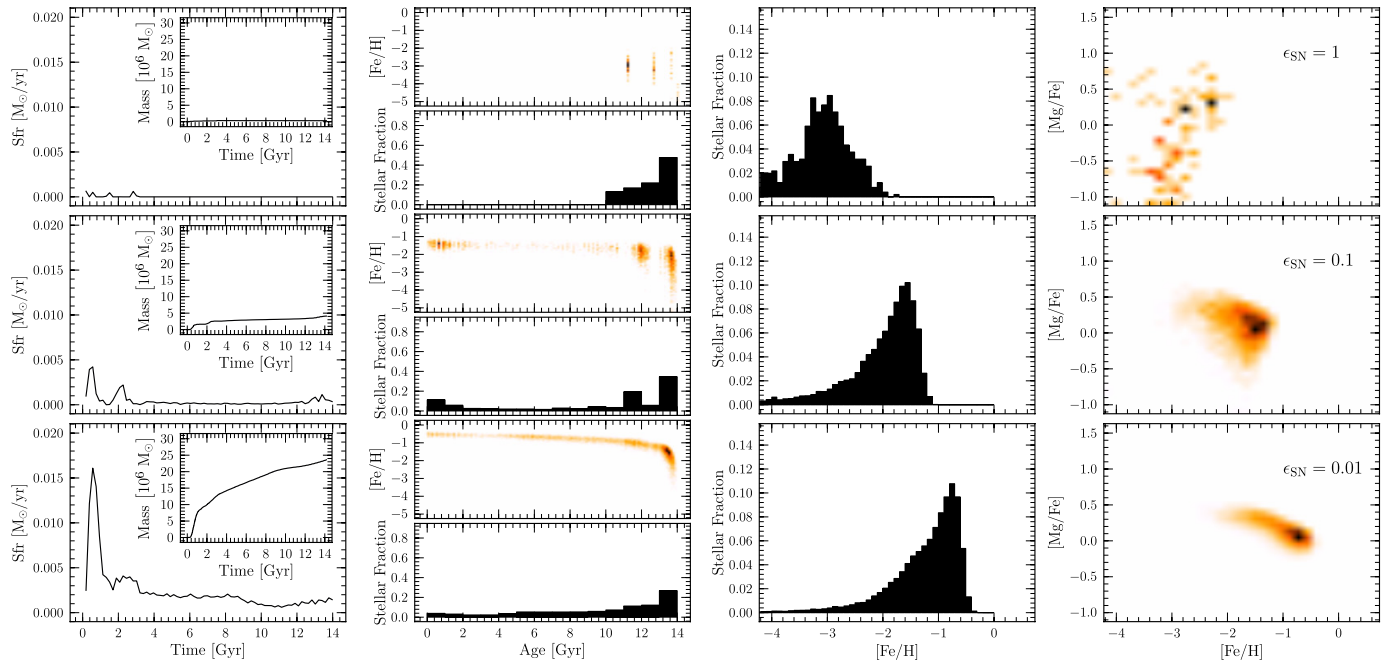

Fig. B.3. Effect of supernova efficiency ϵ_{SN}. The parameters for the initial conditions are $M_{tot} = 6 \times 10^8\, M_\odot$, $\rho_{c,gas} = 0.044\, m_H/cm^3$, and $r_{max} = 8$ kpc. The parameter for the star formation is $c_\star = 0.03$.

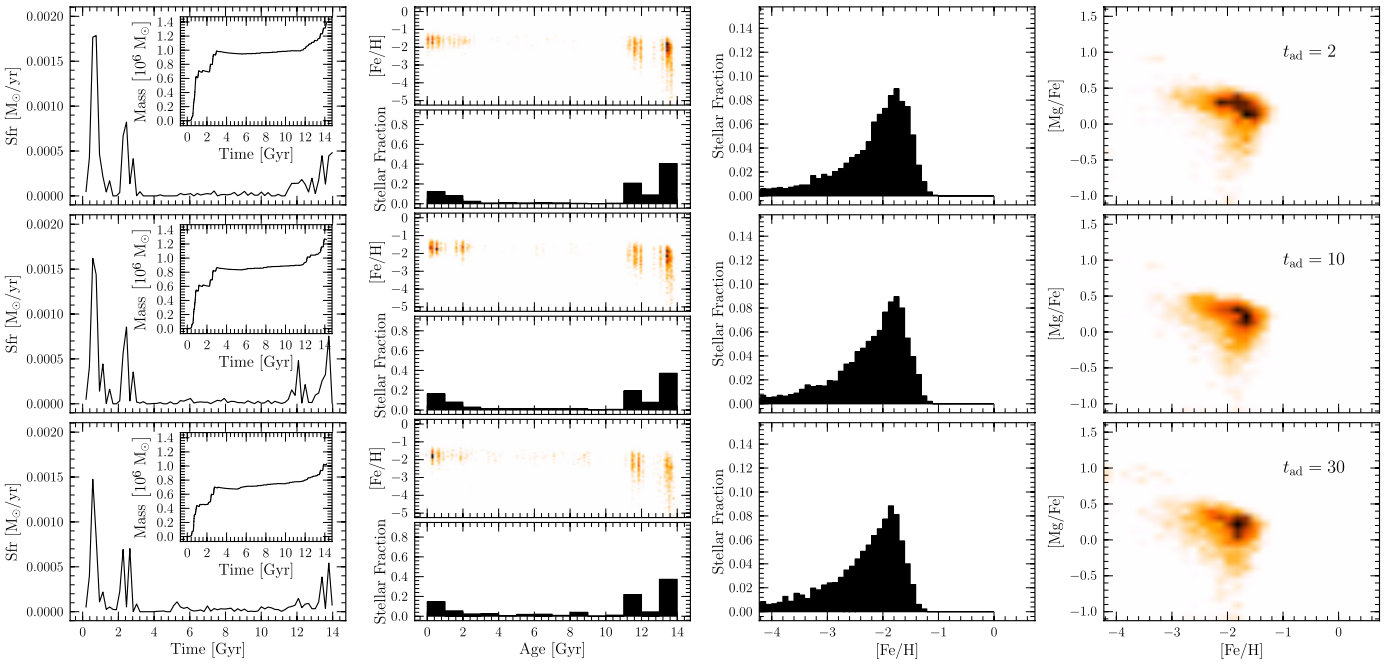

Fig. B.4. Effect of adiabatic time t_{ad}. The parameters for the initial conditions are $M_{tot} = 3.5 \times 10^8\, M_\odot$, $\rho_{c,gas} = 0.025\, m_H/cm^3$, and $r_{max} = 8$ kpc. The parameters for the star formation and supernova feedback are $c_\star = 0.05$ and $\epsilon_{SN} = 0.05$.

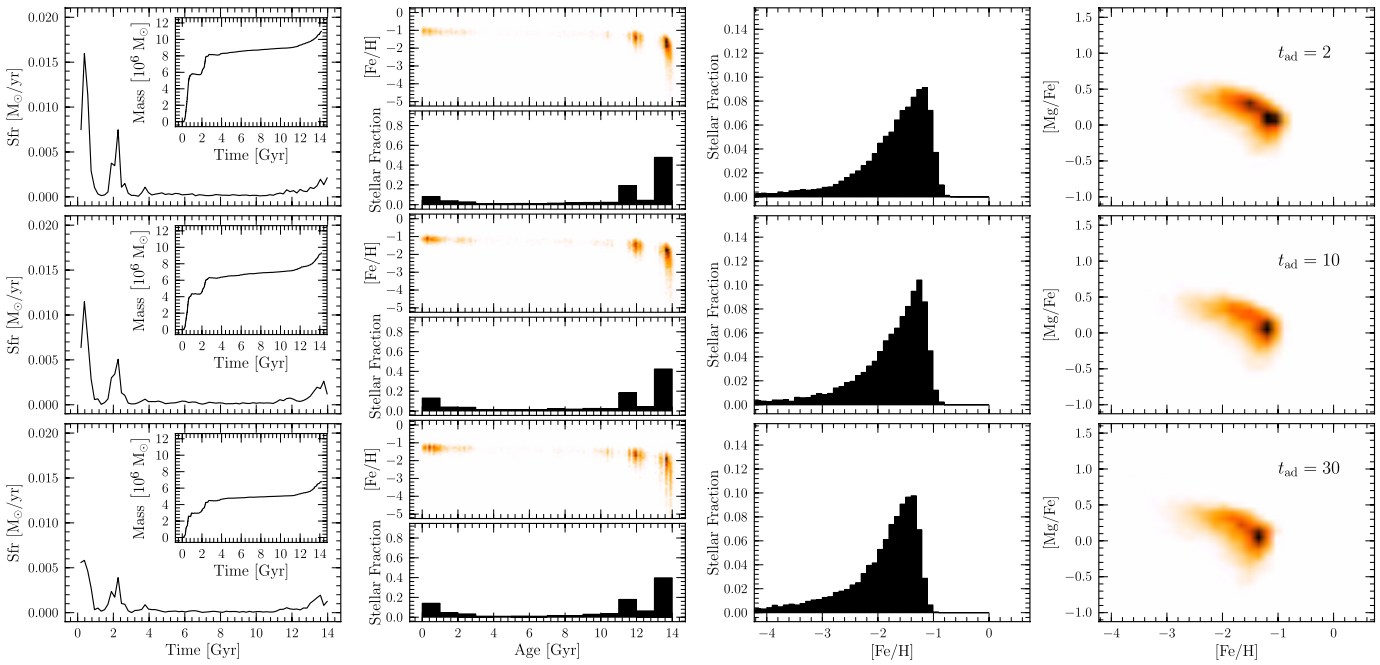

Fig. B.5. Effect of adiabatic time $t_{\rm ad}$. The parameters for the initial conditions are $M_{\rm tot} = 7 \times 10^8\,M_\odot$, $\rho_{\rm c,gas} = 0.053\,{\rm m_H/cm^3}$, and $r_{\rm max} = 8\,{\rm kpc}$. The parameters for the star formation and supernova feedback are $c_\star = 0.05$ and $\epsilon_{\rm SN} = 0.05$.

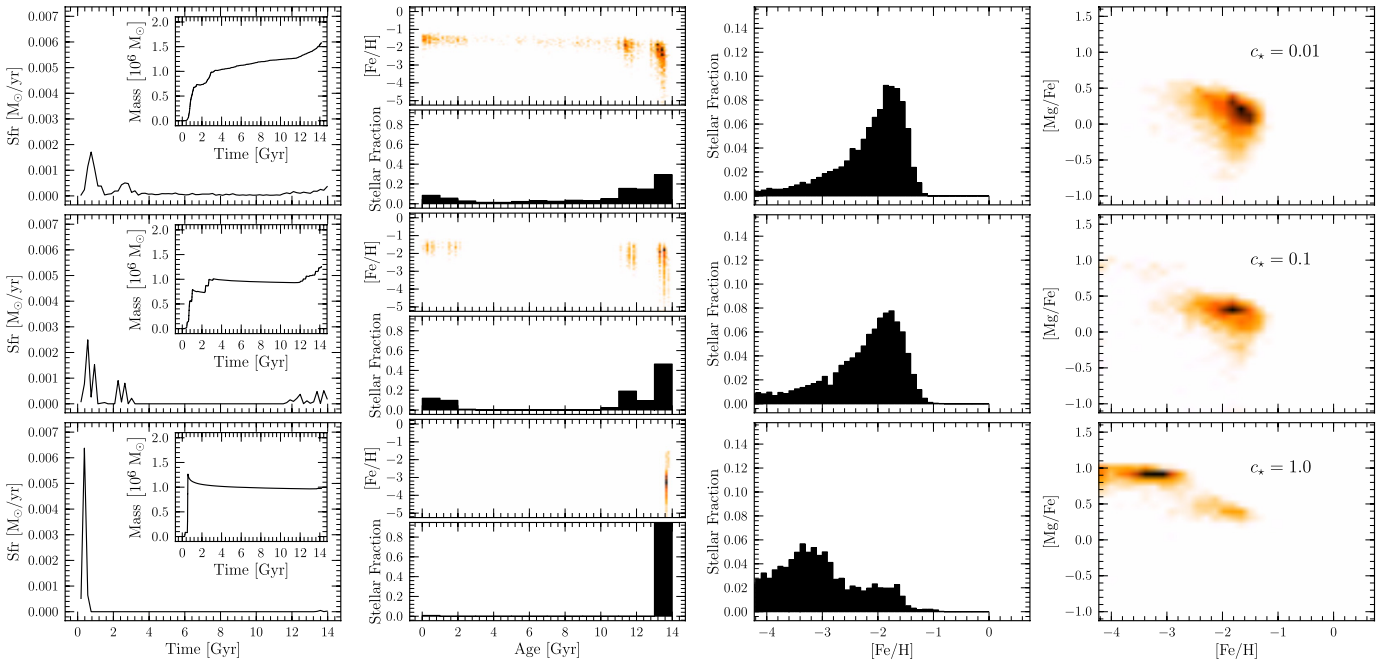

Fig. B.6. Effect of the star formation parameter $c_\star$. The parameters for the initial conditions are $M_{\rm tot} = 3.5 \times 10^8\,M_\odot$, $\rho_{\rm c,gas} = 0.025\,{\rm m_H/cm^3}$, and $r_{\rm max} = 8\,{\rm kpc}$. The parameters for the supernova feedback is $\epsilon_{\rm SN} = 0.05$.

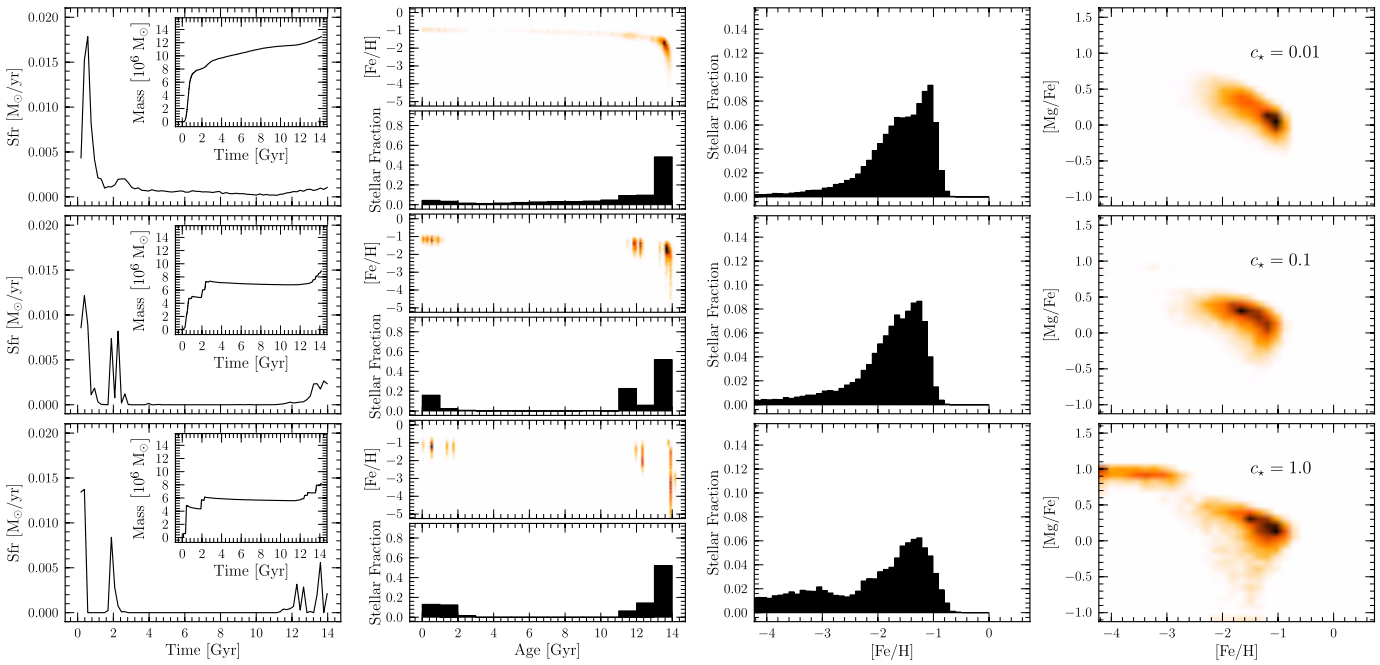

Fig. B.7. Effect of the star formation parameter $c_\star$. The parameters for the initial conditions are $M_{\rm tot} = 7 \times 10^8\, M_\odot$, $\rho_{\rm c,gas} = 0.053\, {\rm m_H/cm^3}$, and $r_{\rm max} = 8\,{\rm kpc}$. The parameters for the supernova feedback is $\epsilon_{\rm SN} = 0.05$.

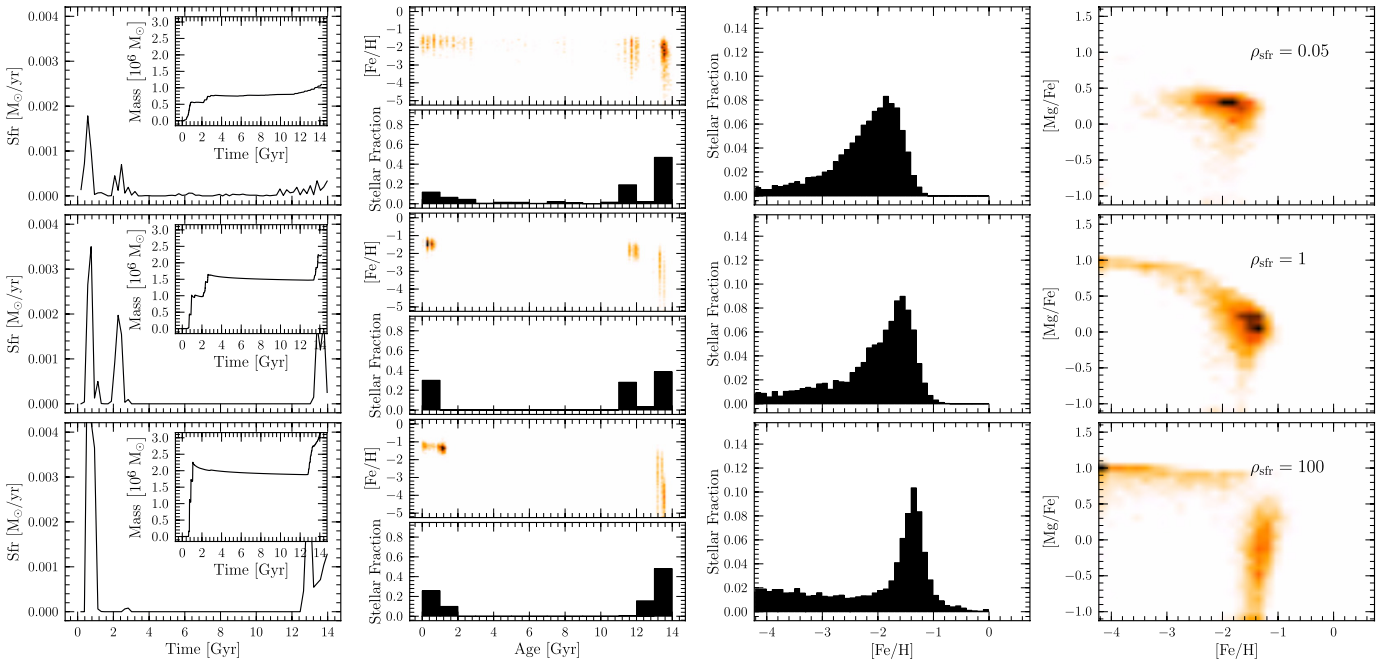

Fig. B.8. Effect of the star formation parameter $\rho_{\rm sfr}$. The parameters for the initial conditions are $M_{\rm tot} = 3.5 \times 10^8\, M_\odot$, $\rho_{\rm c,gas} = 0.025\, {\rm m_H/cm^3}$, and $r_{\rm max} = 8\,{\rm kpc}$. The parameters for the star formation and supernova feedback are $c_\star = 0.05$ and $\epsilon_{\rm SN} = 0.05$.

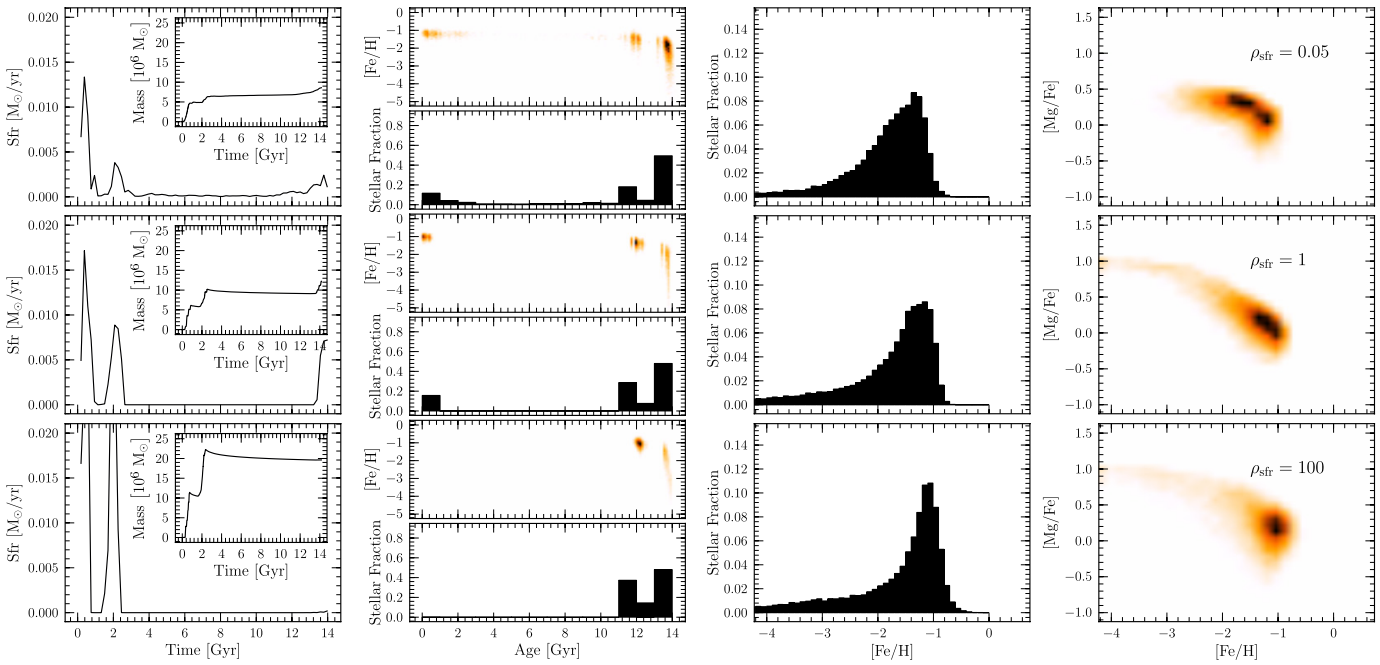

Fig. B.9. Effect of the star formation parameter $\rho_{\rm sfr}$. The parameters for the initial conditions are $M_{\rm tot} = 7 \times 10^8\,M_\odot$, $\rho_{\rm c,gas} = 0.053\,{\rm m_H/cm^3}$, and $r_{\rm max} = 8\,{\rm kpc}$. The parameters for the star formation and supernova feedback are $c_\star = 0.05$ and $\epsilon_{\rm SN} = 0.05$.

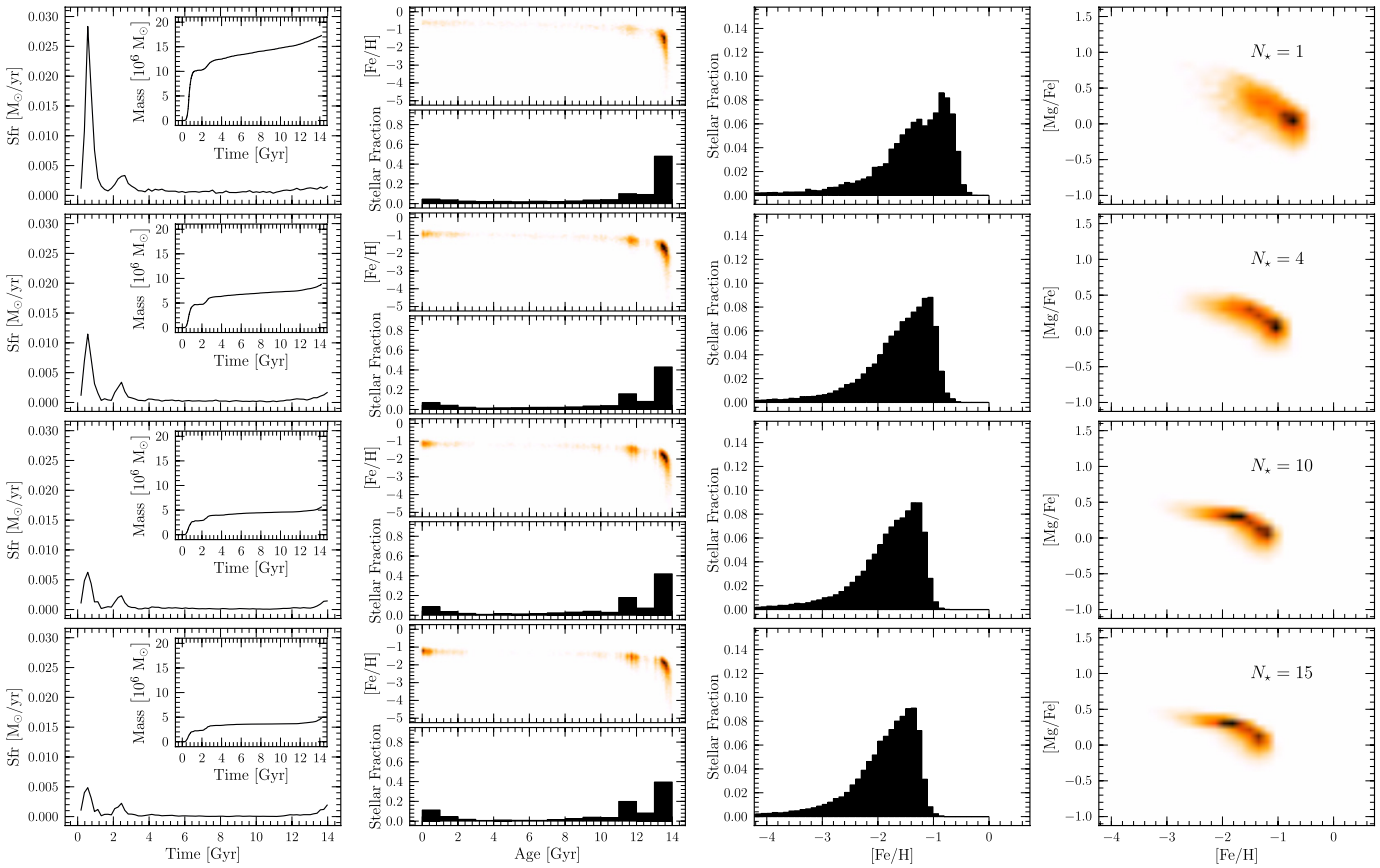

Fig. B.10. Effect of varying the number of stars formed per gas particle $N_\star$. The parameters for the initial conditions are $M_{\rm tot} = 5 \times 10^8\,M_\odot$, $\rho_{\rm c,gas} = 0.037\,{\rm m_H/cm^3}$, and $r_{\rm max} = 8\,{\rm kpc}$. The parameters for the star formation and supernova feedback are $c_\star = 0.025$ and $\epsilon_{\rm SN} = 0.02$.

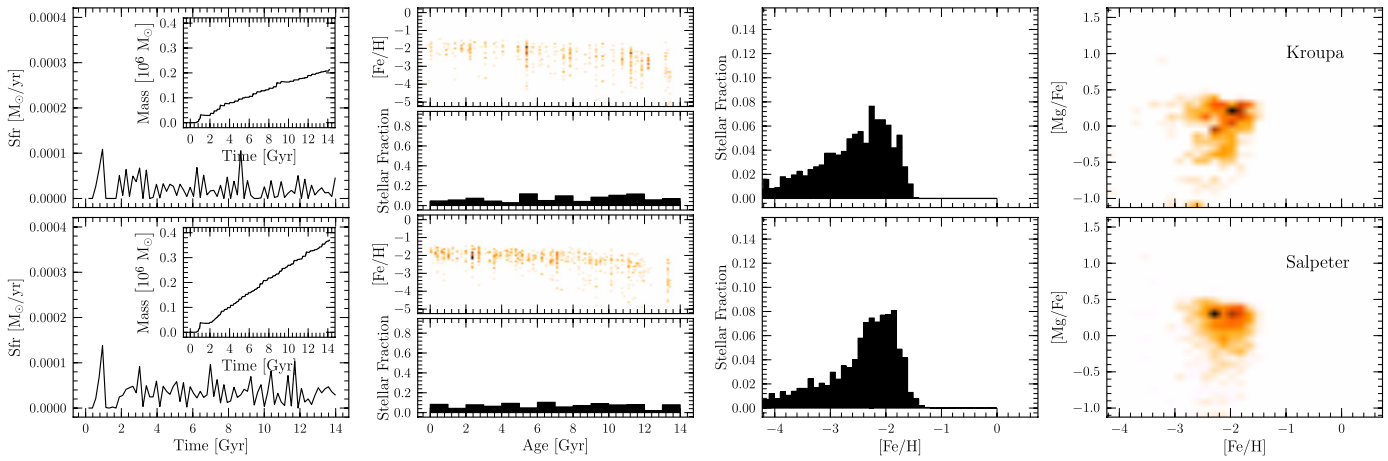

Fig. B.11. Effect of varying the IMF. The parameters for the initial conditions are $M_{\rm tot} = 2 \times 10^8\,M_\odot$, $\rho_{\rm c,gas} = 0.015\,{\rm m_H/cm^3}$, and $r_{\rm max} = 8\,{\rm kpc}$. The parameters for the star formation and supernova feedback are $c_\star = 0.05$ and $\epsilon_{\rm SN} = 0.03$.

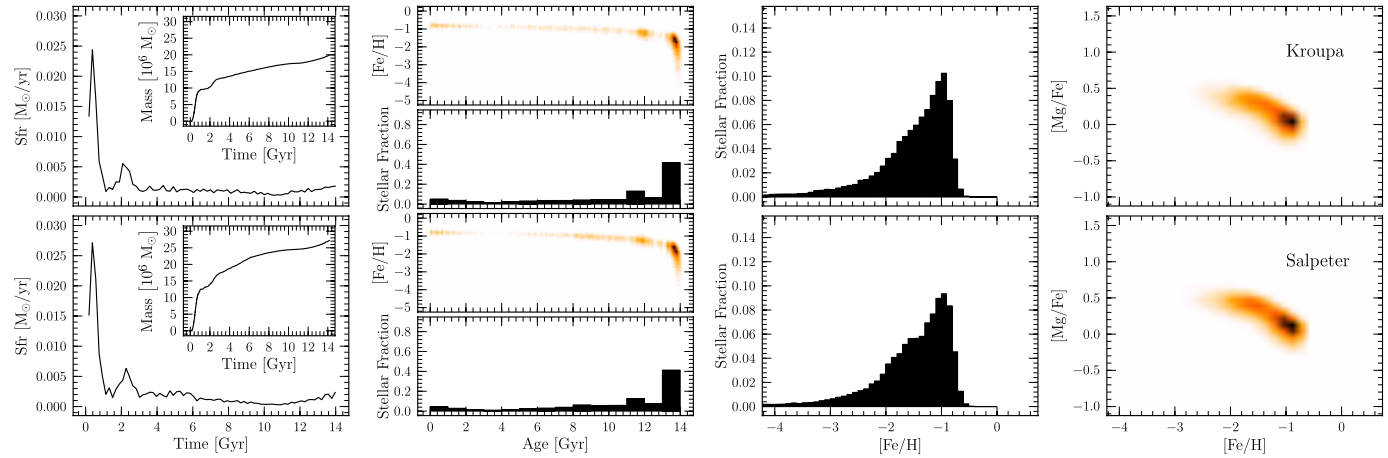

Fig. B.12. Effect of varying the IMF. The parameters for the initial conditions are $M_{\rm tot} = 8 \times 10^8\,M_\odot$, $\rho_{\rm c,gas} = 0.059\,{\rm m_H/cm^3}$, and $r_{\rm max} = 8\,{\rm kpc}$. The parameters for the star formation and supernova feedback are $c_\star = 0.05$ and $\epsilon_{\rm SN} = 0.03$.

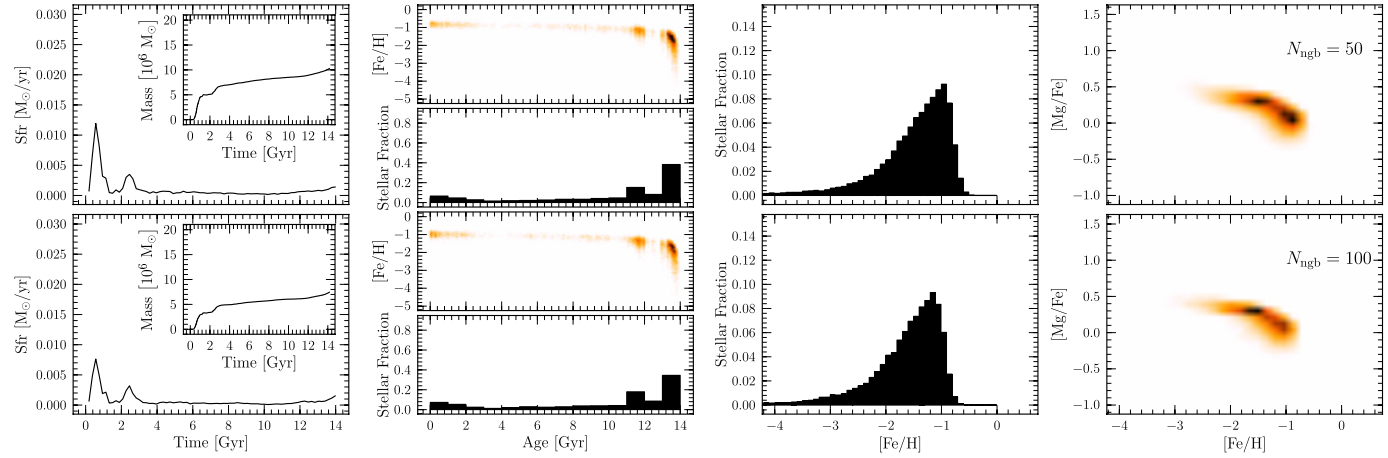

Fig. B.13. Effect of varying the number of neighbors, $N_{\rm ngb}$. The parameters for the initial conditions are $M_{\rm tot} = 4.5 \times 10^8\,M_\odot$, $\rho_{\rm c,gas} = 0.033\,{\rm m_H/cm^3}$, and $r_{\rm max} = 8\,{\rm kpc}$. The parameters for the star formation and supernova feedback are $c_\star = 0.05$ and $\epsilon_{\rm SN} = 0.01$.

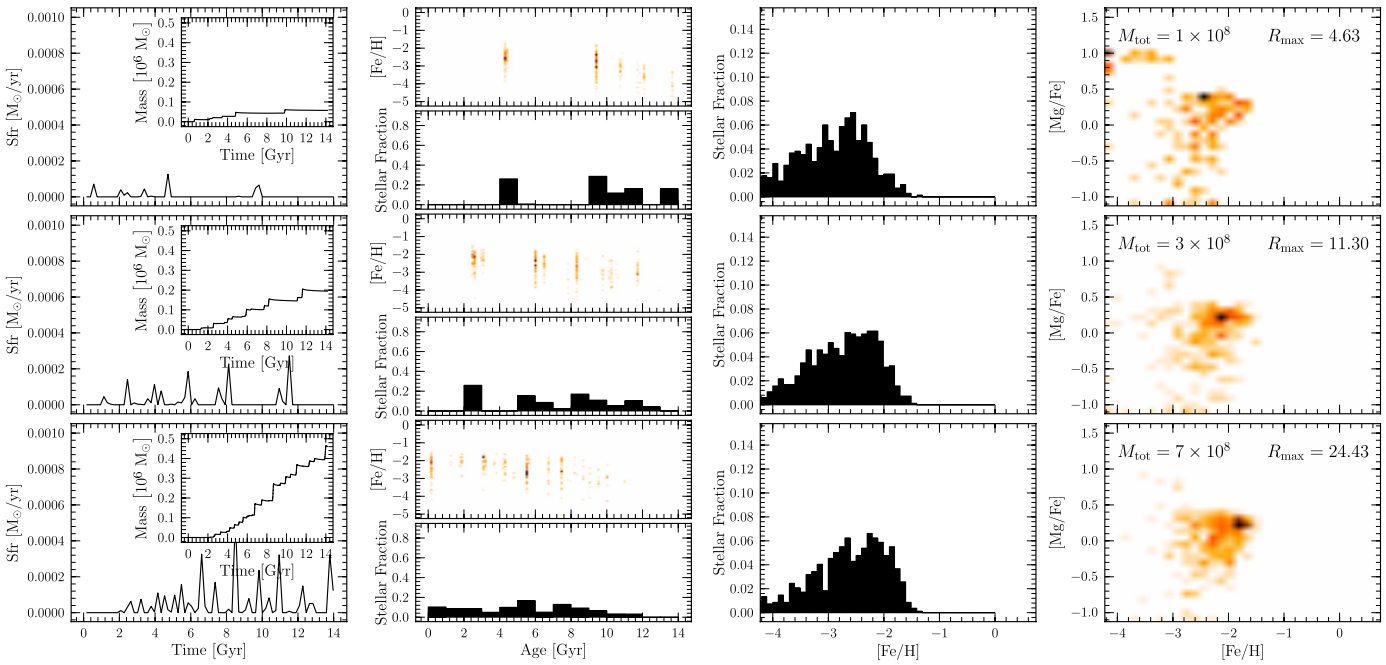

Fig. B.14. Effect of the total mass. We vary $r_{\rm max}$ keeping a constant central gas density $\rho_{\rm c,gas} = 0.015\,{\rm m_H/cm^3}$. The parameters for the star formation and supernova feedback are $c_\star = 0.1$ and $\epsilon_{\rm SN} = 0.05$.

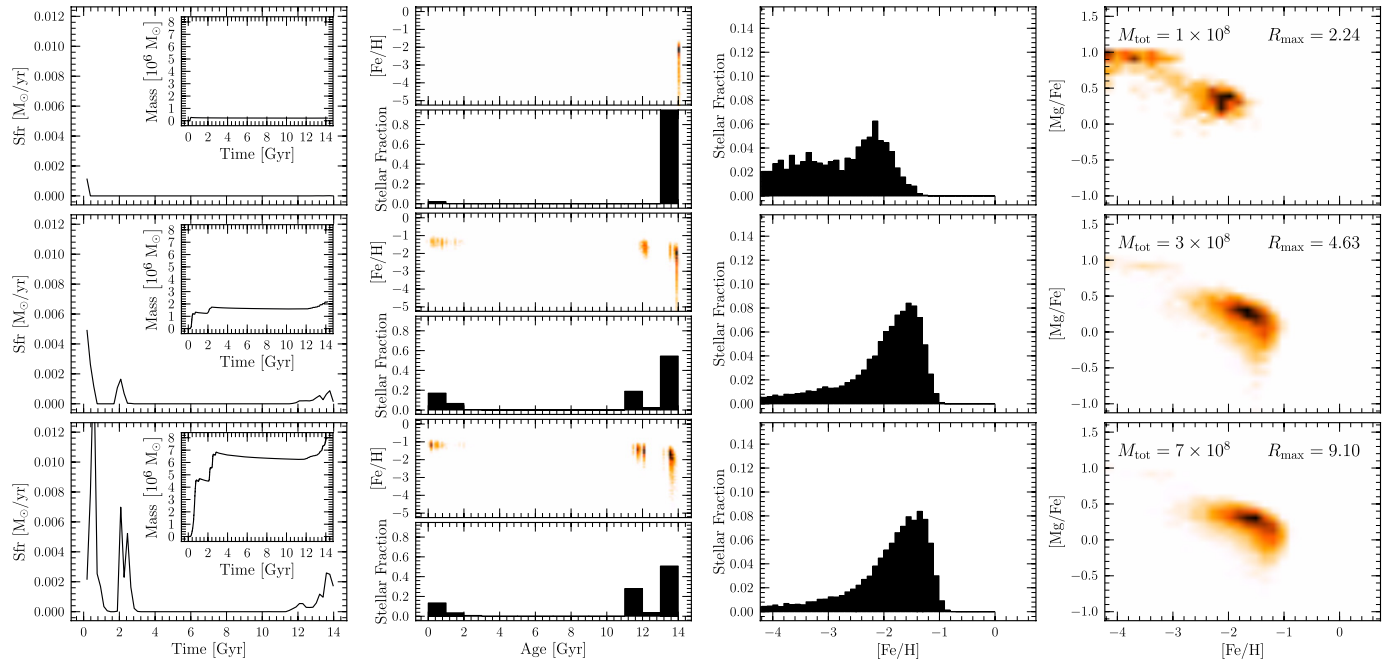

Fig. B.15. Effect of the total mass. We vary $r_{\rm max}$, keeping a constant central gas density $\rho_{\rm c,gas} = 0.044\,{\rm m_H/cm^3}$. The parameters for the star formation and supernova feedback are $c_\star = 0.1$ and $\epsilon_{\rm SN} = 0.05$.

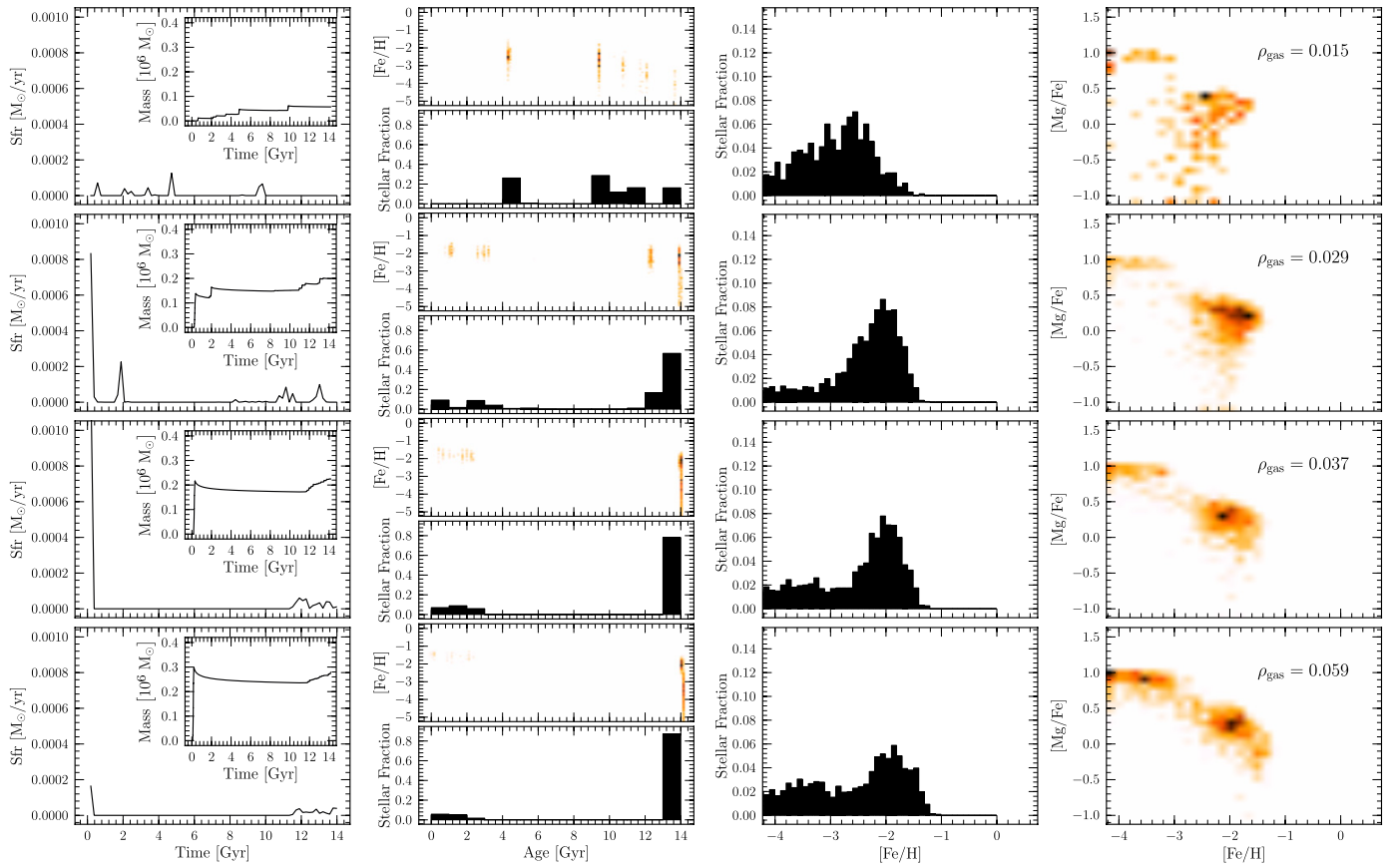

Fig. B.16. Effect of varying the central gas density, for a constant total mass $M_{\rm tot} = 1 \times 10^8\,M_\odot$. The parameters for the star formation and supernova feedback are $c_\star = 0.1$ and $\epsilon_{\rm SN} = 0.05$.

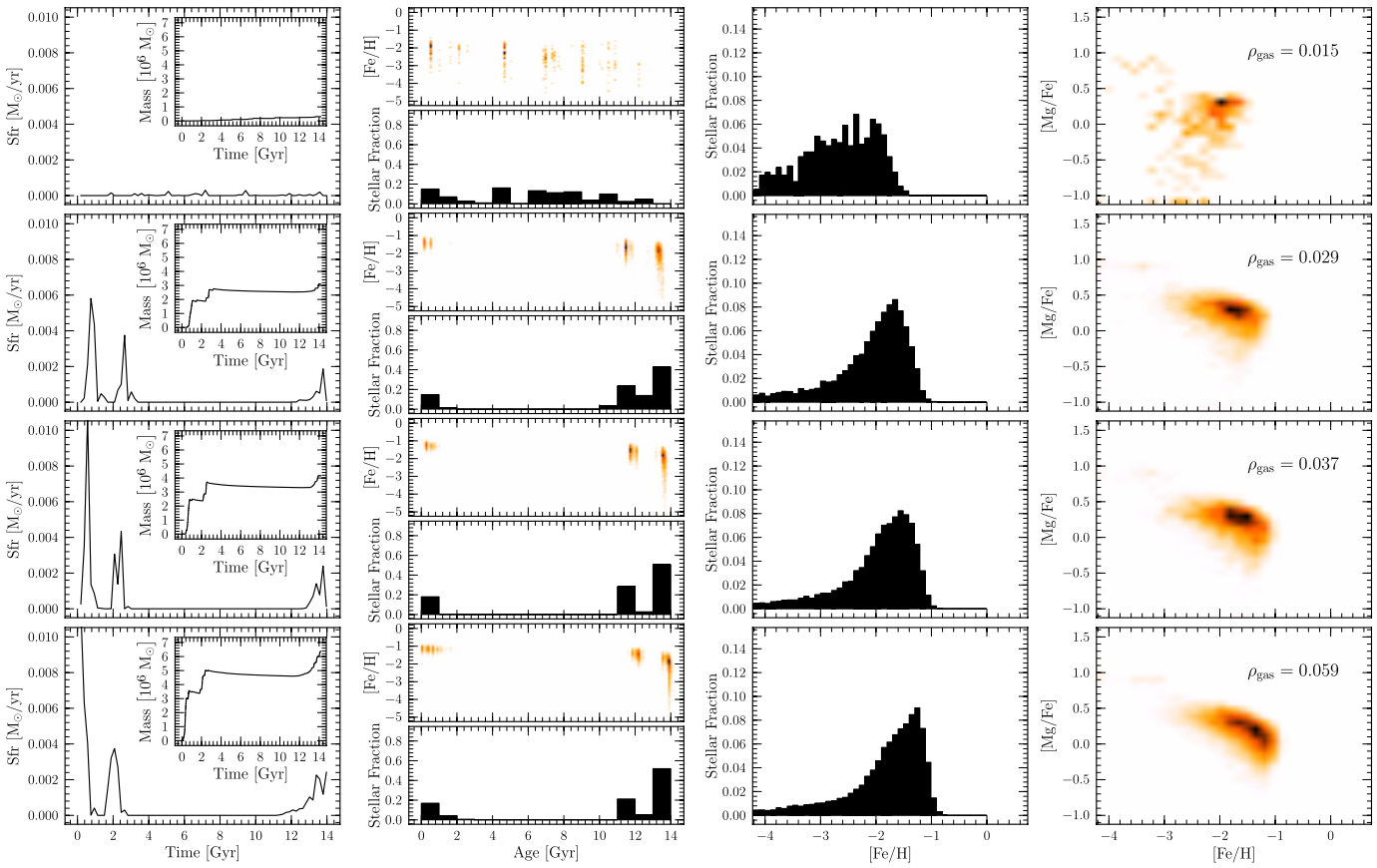

Fig. B.17. Effect of varying the central gas density, for a constant total mass $M_{\rm tot} = 5 \times 10^8\,M_\odot$. The parameters for the star formation and supernova feedback are $c_\star = 0.1$ and $\epsilon_{\rm SN} = 0.05$.